Climate Effects of the Flying V

Master Thesis Report

Matthijs Reekers

Technische Universiteit Delft

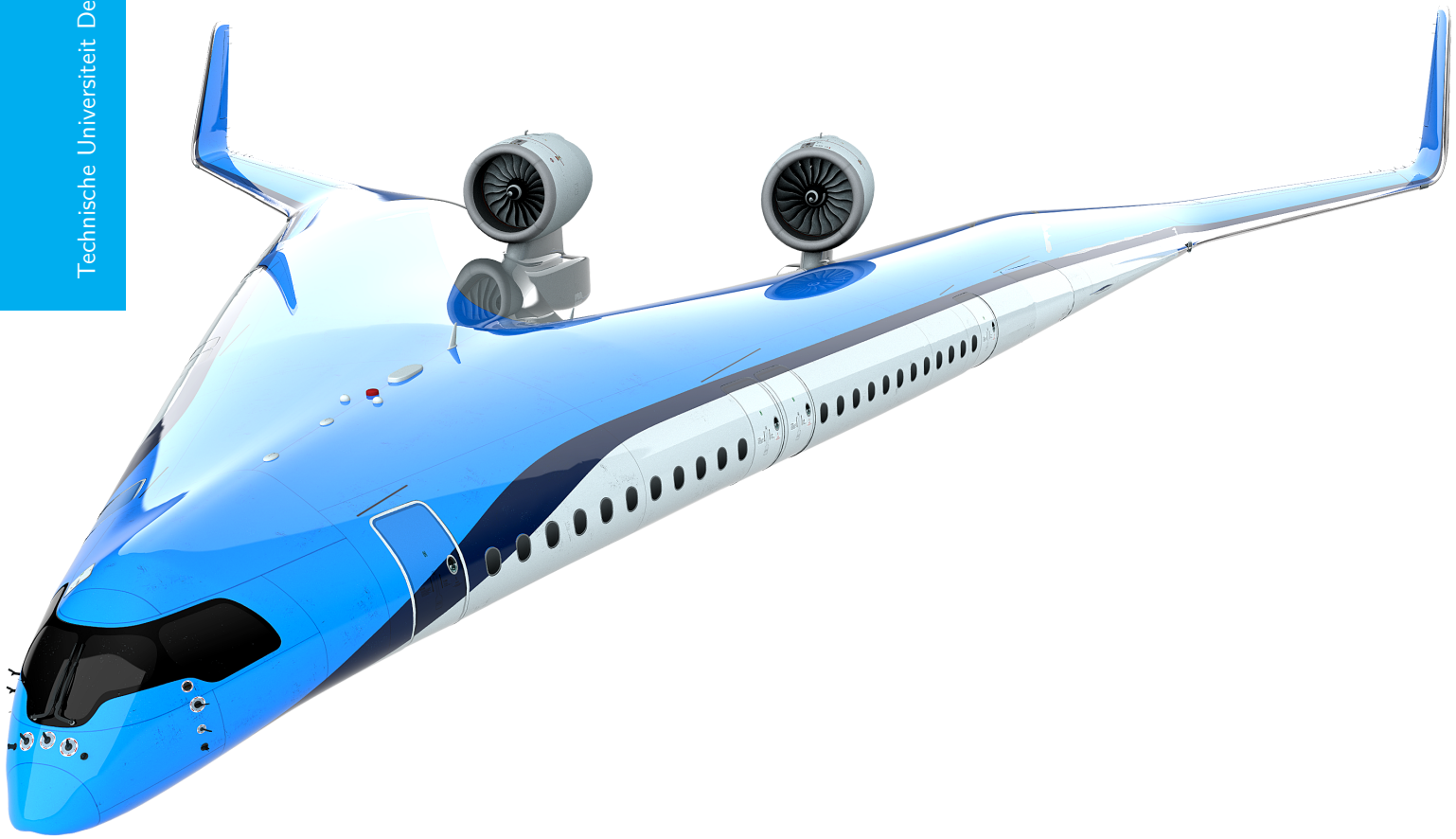

TU Delft Delft University of Technology

Challenge the future

Climate Effects of the Flying V

Master Thesis Report

by

Matthijs Reekers

in partial fulfillment of the requirements for the degree of

Master of Science
in Aerospace Engineering

at the Delft University of Technology,

Student number:	4233905	
Project duration:	June 2020 – June 2021	
Thesis committee:	Dr. F. Yin,	TU Delft, supervisor
	Prof. dr. ir. M. Snellen,	TU Delft
	Dr. ir. R. Vos,	TU Delft
	Dr. I.C. Dedoussi,	TU Delft

TU Delft Delft University of Technology

SUMMARY

Aviation is being recognized as an increasingly important source of anthropogenic radiative forcing. Worldwide economic growth increases the demand for air traffic at a higher rate than technological innovation is able to increase the industry's efficiency. Novel innovative aircraft designs are therefore considered to replace the fleet of conventional tube-and-wing aircraft.

The Flying V is an example of one of such novel concepts, promising a decrease of fuel consumption and the related emission due to superior aerodynamic efficiency and lower weight, which leads to lower fuel consumption compared to a conventional tube-and-wing aircraft such as the Airbus A350. Fuel performance is however not directly proportional to climate impact. The climate impact from non-CO_2 climate species, i.e. NO_x emission, H_2O emission and exhaust contrail formation, varies with their respective location (longitude, latitude and altitude) and time of emission. The Flying V's design altitude is higher than the A350's, so this thesis aims to answer the question whether the Flying V actually outperforms the A350 in terms of climate impact.

Via a literature study, background information has been collected about this topic. Relevant climate agents for this research have been identified. CO_2-effects are relatively easy to quantify. The non-CO_2 effects are caused by H_2O emission, NO_x emission and contrail formation. NO_x emission catalyses O_3 production while it causes atmospheric CH_4 lifetime reduction and background O_3 reduction via primary mode ozone. Contrail formation is caused by hot and humid jet exhaust mixing with cold and dry ambient conditions. These ice-supersaturated conditions lead to ice crystals by condensation of exhaust water vapour over nuclei like soot and aerosol particles which are also present in the exhaust. Over the past decades, the aviation industry's focus has been on reducing fuel consumption, but also operating at higher altitudes, causing more warming effects from the non-CO_2 climate agents.

A methodology has been set up to simulate the climate impact of a given fleet of aircraft, either A350 or Flying V's. Due to dependency of the location and time of emission of the non-CO_2 climate agents, a routing network for the aircraft fleet is necessary. For the city-pairs operating in the network, trajectories can be constructed from any major airport on the globe. These flight paths are made using great circle trajectories from origins to destinations. The fuel mass flow and NO_x emission are computed in a performance model. The performance model computes the drag of the aircraft in cruise conditions. The required thrust is set equal to the drag, from which the required fuel flow is obtained via an interpolated relationship between thrust setting and fuel mass flow. This interpolation is constructed from 4 known thrust settings defined in the ICAO emission databank for the Trent XWB-84 engine, which is used on both aircraft. The NO_x emission is obtained by applying the Boeing Fuel Flow Method 2.

With the aforementioned models, an emission inventory can be constructed, which acts as input for the climate response model AirClim, developed by Volker Grewe [1]. AirClim is able to predict the near surface temperature change over a selected number of years due to a particular emission scenario.

The methodology allowed results to be produced for the two aircraft at their respective design conditions; the design altitude at which they have the best fuel performance and the design Mach number of 0.85. In terms of average temperature response, the A350-900 showed an increase of 2.29 mK, whereas the Flying V-900 showed an increase of 2.31 mK, so a difference of 1% in favour of the A350. The Flying V performed better in fuel performance, yielding lower impact from both CO_2 and NO_x, but seeing increased impact from mainly exhaust contrails, trumping the aforementioned benefits.

Next to this, a sensitivity analysis was performed on the basis of altitude, mach number, location and background scenarios. When varying altitude, it became clear that the Flying V performs better in terms of climate impact if both aircraft fly at the same altitude. Besides, lowering the altitude has a strong positive effect on climate impact for both aircraft. Varying cruise Mach numbers showed minimal change in climate impact.

On a local scale, it became clear that flying at high latitudes (near the poles) cause more than twice as much temperature change per flown kilometer as compared to flying over the tropics. This feature holds for both aircraft.

Next, alternative background scenarios for CO_2, CH_4 and fuel emissions were considered. In the field of climate assessment, assumptions are made regarding future development of CO_2 and CH_4 concentrations

in the atmosphere as well as assumptions for how emission of fossil fuels in general will change over the coming decades. Changing those scenarios changes the net result in climate impact of a particular emission inventory. Results from different scenarios did not show additional discrepancies between the two aircraft.

The uncertainty ranges of the results have been determined by a Monte Carlo simulation. The effects of changing 14 uncertainty parameters have been expressed by recompiling the AirClim software with 10,000 random samples, yielding upper- and lower limits of 1.24 mK and 3.42 mK for the A350-900. The Flying V-900 showed limits at 1.28 mK and 3.43 mK, respectively.

Finally, in an optimization study, the altitude spectrum of both aircraft was drawn downwards even further, to see what happens to the climate impact at altitudes down to 6 km. It became clear that climate impact reduces even further by up to 72% for the A350 and 74% for the Flying V compared to the current design conditions. It should be noted, however, that 6 km altitude is considered extremely low for long range flights.

The main conclusion from this research is that the Flying V is outperformed by the A350 in terms of climate impact if the Flying V operates at higher altitudes. When flying in identical operating conditions, the Flying V outperforms the A350 over the entire operating range. It is therefore recommended to pursue the design of the Flying V at lower altitudes. As for the A350, it is recommended to consider operating the current fleet of A350 aircraft at a lower altitude as well to reduce it's climate impact. These recommendations follow from observations in this research showing that lowering the altitude reduces climate impact, even if this comes with a fuel performance penalty.

The initial focus of this research has been to compare two aircraft, which means that the used methodology would mainly focus on the relative differences between the two aircraft and to a lesser extent on the absolute values and consistency of the results. To validate the recommendation to also operate current aircraft at lower altitudes, it is advised to verify the results and the consistency of the altitude analysis with a different climate model.

PREFACE

This document has been created under unique circumstances. The COVID-19 pandemic has dominated society from the beginning right until the end of this thesis project. At the moment of writing, I still have not had a physical meeting with my supervisor, Dr. Feijia Yin.

Nevertheless, I would like to thank her for ever guiding me through the final stages of my Masters Degree. Her flexibility, theoretical and practical knowledge and critical view have helped me a lot with making this research into a valuable product.

I also want to thank Dr. Roelof Vos, for helping me with specific Flying V and Performance related matters. Dr. Junzi Sun and Prof. Volker Grewe have been incredibly helpful too, by letting me use their software for my research purposes.

Working on this project was done for an overwhelming majority from a home office. Either in my apartment in Rotterdam or at my parents' house in Gouda. I would like to thank my parents, my sister Sophie, her significant other Take and my roommate Ruud for making thesis life more relaxed and more pleasant.

Matthijs Reekers
Rotterdam, June 2021

Contents

List of Figures

List of Tables

NOMENCLATURE

Roman

dT	Temperature change	mK
dt	Time step	s
b_{eff}	Effective wingspan	m
b_{ref}	Reference wingspan	m
e	Oswald factor	-
e_{eff}	Effective Oswald factor	-
ff_{AC}	Fuel flow at sealevel	$\frac{kg}{s}$
ff_{SL}	Fuel flow aircraft	$\frac{kg}{s}$
fp_alt	Pressure altitude	hPa
$fp\_distance$	Flown distance	km
$fp\_distance$	Time frequency	$\frac{1}{year}$
fp_fuel	Fuel burn	kg
fp_lat	Latitude north/south	°
fp_lon	Longitude east/west	°
fp_nox	NO_x emission	kg
g	Gravitational constant	$\frac{N}{kg}$
h	Altitude	m
h_{CR}	Design engine cruise altitude	m
k	Lift-induced drag coefficient factor	-
$l_{winglet}$	Winglet length	m
m	Mass	kg
r	Ratio of temperature and altitude from reference to ambient conditions	-
A_{ref}	Reference aspect ratio	-
C_D	Drag coefficient	-
C_f	Skin friction coefficient	-
C_L	Lift coefficient	-
C_{D0}	Zero-lift drag coefficient	-
$C_{ff,ch}$	Altitude correction factor fuel mass flow	-
C_{ff1}	Polynomial coefficient 1 fuel mass flow	-

C_{ff2}	Polynomial coefficient 2 fuel mass flow	-
C_{ff3}	Polynomial coefficient 3 fuel mass flow	-
D	Drag	N
L	Lift	N
M	Mach number	-
R_{CR}	Cruise range	km
S_{ref}	Wing reference area	m^2
S_{wet}	Wetted Area	m^2
T	Ambient temperature	K
T	Thrust	kN
T_0	Maximum thrust	kN
T_S	Global mean surface temperature	K
V_{TAS}	True airspeed	$\frac{m}{s}$
W	Weight	N

Greek

β	Mach correction factor	-
δ	Pressure ratio	-
γ	Path Angle	$^\circ$
λ	Climate sensitivity parameter	$\frac{K}{Wm^{-2}}$
ω	Specific humidity	-
ρ	Air density	$\frac{kg}{m^3}$
θ	Temperature ratio	-

Abbreviations

ATR	Average Temperature Response	K
BADA	Base of Aircraft Data	
BFFM2	Boeing Fuel Flow Method 2	
EINOx$_{FL}$	NO_x emission index at flight level	$\frac{g}{kg}$
EINOx$_{SL}$	NO_x emission index at sealevel	$\frac{g}{kg}$
ERF	Effective Radiative Forcing	$\frac{W}{M^2}$
FM	Fuel Mass	kg
FW	Fuel Weight	kg
GWP	Global Warming Potential	–
ICAO	International Civil Aviation Organization	
IPCC	Intergovernmental Panel on Climate Change	

ISSR	Ice Super Saturated Region	
OEW	Operational Empty Weight	kg
PMO	Primary Mode Ozone	
PW	Payload Weight	kg
RF	Radiative Forcing	$\frac{W}{M^2}$
RFI	Radiative Forcing Index	–
RFW	Reserve Fuel Weight	kg
RPK	Revenue Passenger Kilometer	pax-km
SAC	Schmidt-Appleman Criterion	
SFC_{CR}	Specific fuel consumption cruise	$\frac{g}{kN-s}$
SFC_{SL}	Specific fuel consumption sea level	$\frac{g}{kN-s}$
TRL	Technology Readiness Level	

1

INTRODUCTION

This chapter elaborates on the underlying problem and the relevance of this research topic. The problem statement is discussed in section 1.1, which leads to the framing of research questions and a research objective in section 1.2. Finally, the outline of this thesis is presented section 1.3.

1.1. PROBLEM STATEMENT

The aviation industry is facing a challenge when it comes to climate impact reduction. The industry is for the most part still dependent on propulsion by combustion engines, burning jet fuels which produce a variety of climate impact.

Greenhouse gas emissions by aviation should be reduced as soon as possible. The industry is investing many resources to accomplish this goal by focusing on alternative design and development of aircraft and propulsion systems, operations and fuels.

The Flying V aircraft is an alternative configuration, which is expected to be more fuel efficient compared to the conventional tube-and-wing configuration. The original concept was proposed by Benad from TU Berlin in 2015 [7]. Currently, TU Delft is working together with Airbus and KLM Royal Dutch Airlines to deliver this design to the industry. A first aerodynamic conceptual design was proposed by Faggiano in 2016 [9]. The past few years, research has been performed from various perspectives to cope with several challenges related to the conceptual design. Currently, a family of Flying Vs is under consideration, with an -800, -900 and -1000 model.

The Flying V designed at TU Delft is expected to reduce fuel consumption by 20% compared to the Airbus A350 while performing a similar mission [7]. This fuel reduction is achieved by a superior aerodynamic efficiency. Like the name suggests, the Flying V is a V-shaped aircraft that no longer contains a conventional fuselage, but merges two fuselage sections with the left- and right wing. This aspect reduces the wetted area of the aircraft significantly, resulting in less drag. A comparison between the novel Flying V and a conventional tube and wing configuration can be seen in fig. 1.1 and fig. 1.2. The key parameters of both aircraft are documented in table 1.1.

Figure 1.1: Flying V

Figure 1.2: Airbus A350-900

As compared to conventional tube-and-wing aircraft, the Flying V is featured with a lower wing loading $\frac{W}{S}$. The reference wing area S_{ref} of the Flying V is higher than for the A350, while the weight W is lower. This lower

Parameter	A350-900	Flying V-900
Maximum Take-off Weight	280 t	244 t
Operational Empty Weight	142.4 t	120 t
Passengers	315	315
Cargo capacity	172.4 m^3	160 m^3
Fuel capacity	138 000 L	129 000 L
Wing Area	442 m^2	860 m^2
Design Range	15 000 km	14 800 km
Cruise Mach Number	0.85	0.85

Table 1.1: Key parameter comparison A350 and Flying V

wing loading implies that the aircraft generally needs to fly at higher altitudes or at lower speeds to achieve optimal flight performance. However, flying at higher altitude also influences the impact of the various climate effects from combustion emissions and contrails formed at the engine exhaust. Recent studies have shown that the non-CO_2 effects, mostly nitrogen oxide emissions, water vapor emissions and and contrail formation are highly dependent on geographical location, altitude and of emission [10].

The location and altitude dependency of non-CO_2 effects raises the question whether the Flying V concept is actually as much of an improvement in terms of climate impact as it promises to be and if not, which climate impact mitigation strategies would be feasible for this type of aircraft.

1.2. RESEARCH QUESTIONS AND SCOPE

This report contains a detailed description of the thesis research project concerning the climate impact of the Flying V aircraft. At the beginning of the project, a research question was stated to be answered over the course of the thesis. The research question to be answered in this thesis is:

> *How does the Flying V aircraft perform in terms of climate impact and mitigation capabilities compared to a conventional tube-and-wing aircraft?*

For both the Flying V and the conventional tube-and-wing aircraft, the following sub-questions have been formulated:

1. What is the full set of climate effects related?
2. What is the current predicted climate impact in terms of near surface temperature change for a given fleet of aircraft?
3. What is the change in climate impact when varying cruise speed?
4. What is the change in climate impact when varying altitude?
5. What is the change in flight performance when varying cruise speed?
6. What is the change in flight performance when varying altitude?

The main research objective of this thesis is:

> "To do a climate assessment of the Flying V aircraft and the Airbus A350, by means of simulations"

This thesis research is a typical case study between a novel concept and it's conventional counterpart. In this particular project, the A350-900 will be the baseline aircraft, to which the Flying V-900 is compared. The aim of the methodology is to make a framework that can make comparisons of different aircraft as well.
The design of any of the Flying V variants remains untouched in this thesis. The climate impact and performance of the design will be critically analyzed such that conclusions and recommendations can help in a future redesign cycle of the Flying V project.

1.3. THESIS OUTLINE

This research has been performed in three phases:

- Literature study
- Climate assessment approach
- Results interpretation

The literature study phase, elaborated in chapter 2, served as a way to familiarize with several fields of research that may be relevant to this topic. The climate assessment approach phase is discussed in chapter 3. It describes the methods used and tools built over the course of this research to serve the climate assessment goal of this research. These results are interpreted in the final phase and shown in chapter 4. Finally, chapter 5 discusses the conclusions and recommendations that seal this thesis project.

2

BACKGROUND

This chapter elaborates on the literature that has been relevant throughout this research. The aforementioned literature study emphasized on 5 topics:

- Climate effects of aviation, discussed in section 2.1
- Climate effects and aircraft design, discussed in section 2.2
- Climate modeling, discussed in section 2.3
- Performance modeling, discussed in section 2.4
- Features of the Flying V, discussed in section 2.5

A brief overview of these topics will be elaborated in this chapter. These topics are elaborated in more detail in the literature study report [11].

2.1. CLIMATE EFFECTS OF AVIATION

Aviation is estimated to be responsible for 5% of anthropogenic radiative forcing , which causes global warming. This was determined by the Intergovernmental Panel on Climate Change (IPCC) in their Fourth Assessment Report [12]. Aviation is one of a few industries where climate impact is expected to increase in the future. The COVID-19 pandemic has caused a temporary decline in air traffic, but eventually the growth of the aviation industry is expected to recover according to the Boeing Commercial Market Forecast [1]. The International Civil Aviation Organization (ICAO) forecasts an annual air traffic growth of 4.3% until 2035, and 4.1% towards 2045 [13]. Aviation is still almost completely dependent on fossil fuels, leading to the conclusion that climate impact by aviation is expected to grow parallel to the growth in air traffic. The aforementioned 5% represents an estimation of the full set of climate agents, both CO_2 and non-CO_2. An overview of the overall impact of the climate agents is shown in fig. 2.1. The next subsections will elaborate on the different climate agents CO_2, water vapour, NO_x, contrails and aerosols.

2.1.1. CARBON DIOXIDE

CO_2-effects are relatively well known and easy to quantify. Carbon dioxide emissions are directly proportional to the fuel burn by aircraft engines. CO_2 mixes with air, changing the atmospheric CO_2-concentration and produces a direct warming effect by absorbing infrared radiation from the surface of the Earth. The rate of emission is generally around 3.15 kg per kilogram of kerosene when assuming complete combustion. CO_2 emissions and their effects are independent of flight phase or operating condition due to their long life cycle.

The long lifetimes causes cumulative emissions over time to determine the change in CO_2 concentrations in the atmosphere, so the entire history of emissions down to the 1940s is generally used in modeling carbon dioxide climate impact [14].

[1] https://www.boeing.com/commercial/market/commercial-market-outlook/

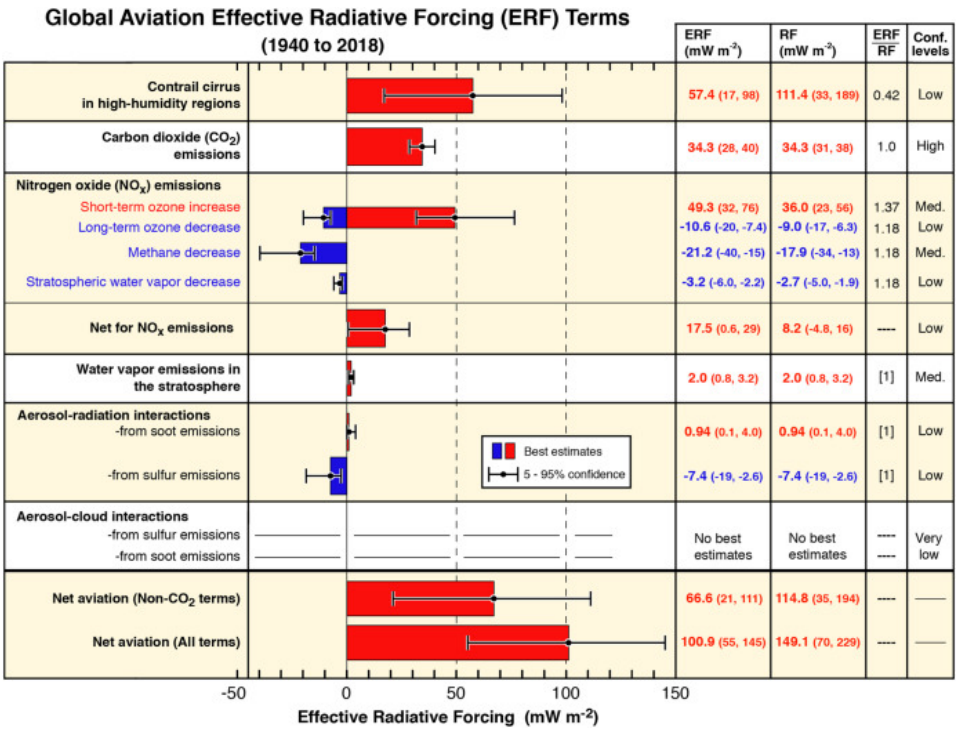

Figure 2.1: Radiative forcing components [2]

2.1.2. WATER VAPOUR

Water vapour is another product of hydrocarbon fuel combustion. Water vapour is a natural greenhouse gas, which is regulated by the hydrological cycle. Additional water vapour concentration in the atmosphere due to emissions is generally small compared to the natural amount.

However, a climate assessment study by Lee et al in 2010 [15] projected a high uncertainty regarding water vapour emissions with an upper bound of 20.3 $\frac{\text{mW}}{\text{m}^2}$, which is a similar order of magnitude as compared to the estimated radiative forcing from CO_2, NO_x and contrails. More recent studies such as Wilcox et al in 2012 [4], concluded that radiative forcing of that order of magnitude due to water vapour emission is not plausible. The upper bound of the radiative forcing originates from the assumption that the uncertainties in the water vapour forcing follow a log-normal distribution and from a choice of a somewhat arbitrary near-zero lower limit to this forcing. So it does not originate from a detailed assessment of individual sources of uncertainty. Lee et al re-assessed climate impact from water vapour emissions in 2021 [2] where the upper bound of uncertainty was also concluded to be much lower.

It should also be noted that the generally low climate impact predictions hold for the current fleet of aviation, where subsonic flight at lower altitudes is predominant. When supersonic flight at higher altitudes is introduced, the effects of water vapour emission are expected to become much more significant [16].

2.1.3. NITROGEN OXIDES

Emission of Nitrogen Oxides (NO_x), either in the form of Nitric Oxide (NO) or Nitrogen Dioxide (NO_2), play a large role in the production of ozone (O_3), which is another greenhouse gas. NO_x emissions arise from the combustion process when atmospheric nitrogen reacts with oxygen under high temperature and pressure conditions in a gas turbine combustion chamber [17]. NO_x emissions act as a catalyst in the formation of ozone, where OH^- is one of the products of a complex chemical process. OH^- reacts with methane, resulting in a reduction of background methane and background ozone production [18], causing a cooling effect. This secondary cooling effect is also called Primary Mode Ozone (PMO). The resulting radiative forcing due to NO_x emissions is however generally positive, causing an overall warming effect.

2.1.4. CONTRAILS

Condensation trails, often abbreviated to contrails, are line shaped clouds that are either produced by engine exhaust or by a pressure change over an airframe. The latter contrail type is also referred to as aerodynamic

contrails. Contrails can become persistent and evolve into induced cloud cirrus, resulting in a radiative forcing effect. Whether this radiative forcing effect is negative or positive depends on the location in the atmosphere and the time of emission. Daytime contrails both reflect sunlight back into space causing a negative radiative forcing and reflect infrared radiation back to the surface of the earth causing a positive effect. Nighttime contrails only reflect infrared radiation back to the surface of the earth due to the absence of sunlight. Contrails therefore cause both heating and cooling of the surface of the earth during the day and heat the surface during the night. The net result of contrails therefore depends on daily variation of natural cloud coverage, but the general scientific consensus is that contrails overall cause a positive radiative forcing effect [12].

EXHAUST CONTRAILS

Exhaust contrails form when hot and humid exhaust air from a jet engine mixes with much drier and cooler free-stream air at cruise altitudes. This mixing mechanism constantly reduces temperature and increases humidity of the surrounding air, which causes saturation of the air with respect to liquid water, forming droplets. When conditions are cold enough, generally lower than -38 degrees Celsius, supercooled droplets freeze and contrails form.

Whether an exhaust contrail forms and persists is determined by the Schmidt-Applemann Criterion [19], or SAC. The SAC states that three conditions need to be satisfied for formation of persistent contrails:

- The relative humidity for water should be lower than 100% for water
- The relative humidity for ice should be higher than 100% for water
- Ambient temperature should be below -38 ° C

The properties of exhaust contrails is dependent on the amount particle emissions in the jet plume, such as soot. Soot particles allow water vapour from a super-saturated atmosphere to condense to form ice crystals [20]. A higher amount of soot particles in the jet plume leads to a higher amount of ice particles in the contrails and vice versa.

When a persistent contrail is formed, it may spread to form an extensive heterogeneous cloud structure by merging into another [21]. This is called 'contrail-cirrus', due to the similarities between this phenomenon and natural cirrus.

AERODYNAMIC CONTRAILS

This type of contrail is formed under a pressure and temperature drop over a lifting body. In humid conditions, this temperature drop can trigger formation of clouds through condensation of the humid air. Usually, this type of contrail dissipates within a few seconds after formation.

The ideal conditions for formation and persistence of aerodynamic contrails at cruise altitudes are humid and relatively warm conditions, as long as the temperature is below the condensation threshold [22]. The contrails need high temperatures to form stable ice crystals capable of developing into contrail cirrus from supersaturated air masses. These conditions are rare and mostly present in the atmosphere above the tropics. The tropic latitudes see the biggest increase in air traffic, so the relevance of aerodynamic contrails in terms of climate impact can increase in the future, though currently, the predicted impact of these phenomena are small compared to those of exhaust contrails.

2.1.5. AEROSOLS

Aircraft emit aerosols in the form of sulphate and soot. Kerosene can contain sulphur (S) which is oxidised to sulphur dioxide (SO_2) during combustion [23] and then converted into sulphuric acid (H_2SO_3) [21]. Sulphuric acid either forms or is able to form a coating around existing particles. These particles act as a reflector of solar irradiance back into space, thus providing negative radiative forcing. This cooling effect is however limited due to the fact that the sulphur concentration in jet fuel is limited by regulations to avoid undesirable phenomena such as acid rain.

Soot refers to non-volatile black carbon emissions from aircraft. Soot is a result from incomplete combustion and is generally measured as 'smoke number'. Soot has a direct positive radiative forcing effect, because the black carbon particles trap infrared radiation [24]. The emission index of black carbon is relatively small, so the direct positive radiative forcing is small.

There is however a secondary effect in the form of linear contrail formation and aviation induced cloudiness, which are discussed in section 2.1.4. This effect is suspected to be large although the quantification of

this effect contains many uncertainties, due to unreliable assessment of black carbon emissions and incomplete understanding of how these particles interact with clouds.

2.2. CLIMATE EFFECTS AND AIRCRAFT DESIGN

This section elaborates on the relationship between aircraft design and climate effects. Section 2.2.1 discusses the trends of aircraft design with respect to fuel efficiency. Next, section 2.2.2 will contain theory regarding the sensitivity of climate impact with regards to an aircrafts' operating conditions. Finally, section 2.2.3 will explain the climate impact mitigation strategies that have generally been considered in the aircraft industry.

2.2.1. DESIGN TREND

Like any other industry, aircraft design has ever focused on achieving maximum efficiency; transporting a certain payload with the lowest possible amount of fuel burnt and the lowest amount of time spent. Innovations in the past have led to significantly more efficient aircraft configurations and aircraft engines.

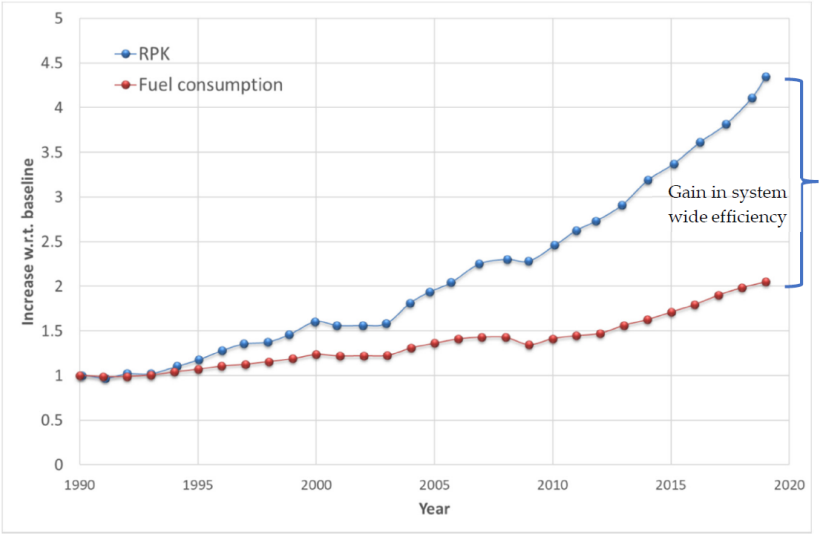

Figure 2.2: RPK and fuel consumption development since 1990 [3]

Figure 2.2 demonstrates the development of air traffic in Revenue Passenger Kilometers (RPK) and fuel consumption since 1990. Air traffic has grown by a factor 4.3, while the fuel consumption has only doubled, implying a system wide gain of 115% in terms of efficiency.

Motivations for increasing aircraft efficiency are particularly related to cost. Lower amounts of fuel burn mean lower ticket prices for the passengers. Additionally, less fuel burn implies less emissions and thus less climate impact. The latter statement is not necessarily true, though. This has to do with climate impact from non-CO_2 effects at higher altitudes, which will be discussed next.

2.2.2. ALTITUDE SENSITIVITY

Several climate effects show a dependency with an aircraft's operating conditions. The aviation industry has also invested many efforts to fly faster in order to reduce the flight time, which reduces the operating cost of a certain flight and pleases the passenger who's travel time is kept to a minimum. These faster aircraft need to cruise at higher altitudes in order to achieve maximum aerodynamic efficiency. Flying at these higher altitudes comes with side effects in the form of additional radiative forcing mainly due to NO_x emissions, water vapour emissions and the formation of exhaust contrails. These side effects are generally increasing radiative forcing, which is emphasized by the following figures.

Figure 2.3 shows the global-mean radiative forcing per Tg of input water vapour emissions per month as a function of emission height. A clear quasi-linear trend is distinguished concluding that radiative forcing from water vapour increases with altitude. The kink, which occurs between 9,500 and 10,000 m altitude, is most likely caused by the presence of the tropopause. The slope of the impact from water vapour emissions may change due to different ambient conditions above and below the tropopause.

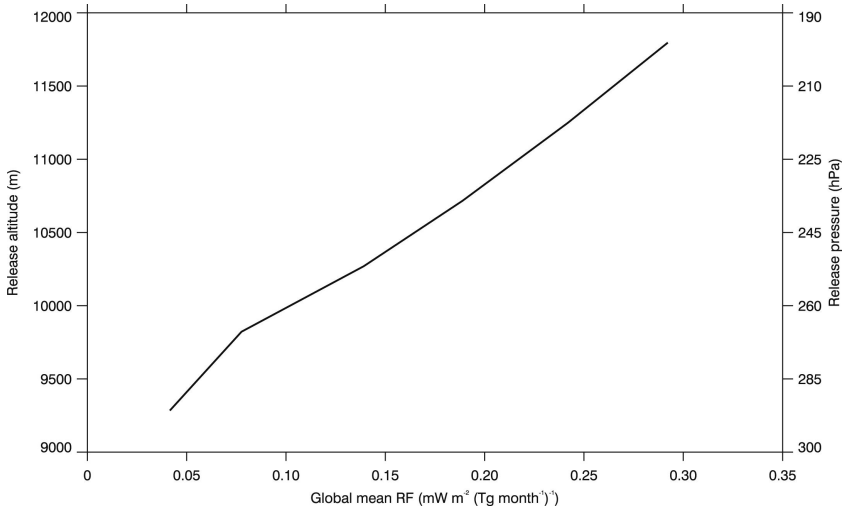

Figure 2.3: Water vapour RF as function of altitude [4]

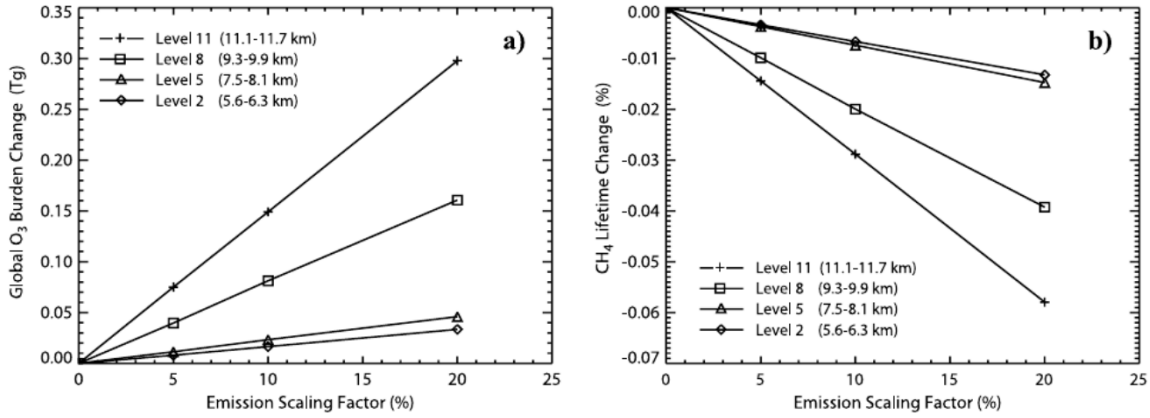

Figure 2.4: Linear response O_3 (a) and CH_4 (b) with NO_x emission scaling factor [5]

Figure 2.4 shows that NO_x emission released at higher altitudes causes both increased O_3 burden, but also an decreased CH_4 lifetime change. The O_3 burden is of higher significance however, resulting in a higher net climate impact from NO_x emission at higher altitudes.

Figure 2.5 shows the distances flown globally per altitude, both total distance and distance through so called Ice Super-Saturated Regions (ISSR). ISSRs are locations in which the formation of persistent contrails is most effective, causing the most burden from exhaust contrail radiative forcing. It is visible that the highest concentration of kilometers flown through ISSR are at higher altitudes, especially in the current flight corridor between 8 km and 12 km altitude.

The counteracting climate effects following from more efficient aircraft at higher altitudes require trade-offs in future aircraft design. Schwarz and Kroo performed a case study discussing this trade-off in 2009 [25]. This study investigated for both a short range narrowbody and a long range widebody aircraft how the design of an aircraft changes with respect to cost, fuel burn, NO_x emissions and the overall climate impact. For each of these four features, an aircraft design was generated with corresponding cruise altitude and cruise speed. The correlation between these two operating conditions and climate impact was very distinct: climate impact drastically decreases when designing for lower cruise altitudes and lower cruise speeds.

2.2.3. MITIGATION

Mitigation of climate impact by technological or operational modifications require full consideration of CO_2 and non-CO_2 effects. Increasing combustor temperatures and pressures has positive effect on fuel efficiency and therefore decreases CO_2 emission. This comes however with increased NO_x emissions. NO_x emissions

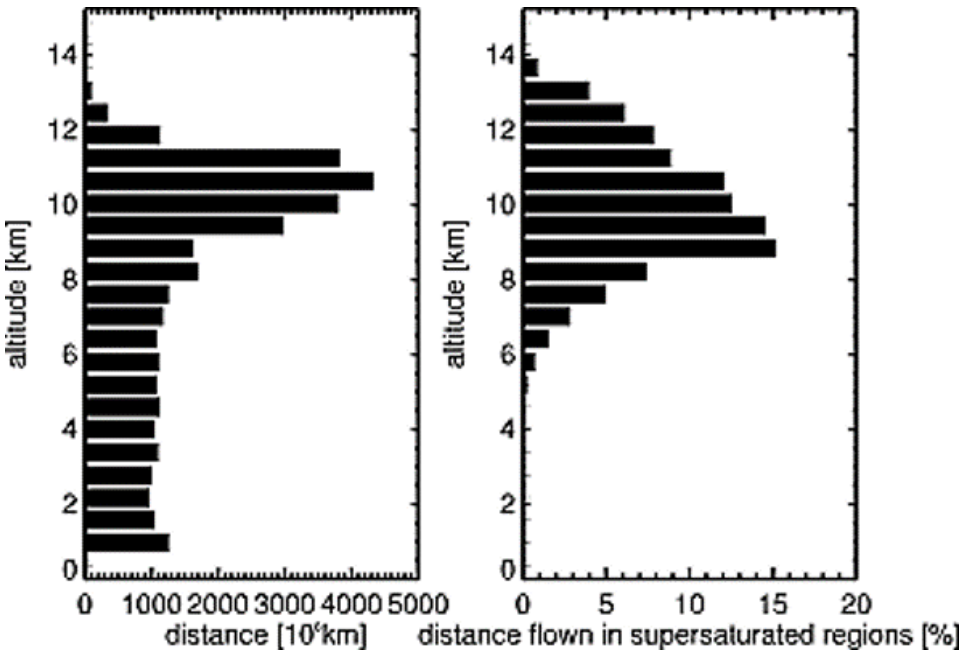

Figure 2.5: Global kilometers flown, total and through ISSR [6]

can vice versa be reduced at the expense of a higher fuel burn and thus a higher CO_2 emission. In order to prevent the NO_x emission penalty, combustion technology needs further development, such as the use of LO-NO_x burners [26].

A similar trade-off situation exists for CO_2 and contrail cirrus. Avoiding ISSRs by flying under, over or around them may result in reduced radiative forcing from contrails. This however comes at the expense of additional fuel burn, yielding higher cost and more emitted CO_2.

2.3. CLIMATE ASSESSMENT OF AVIATION TECHNOLOGY

Climate modeling methods have been investigated, with most emphasis on AirClim, a climate-chemistry model requiring very low computational effort. Uncertainties in modeling have been a challenge in this field of research, and with AirClim, this challenge remains. More details regarding the AirClim software will be discussed in section 3.4.1. Alternatives to AirClim have been considered, but they have been omitted as feasible options for the following reasons:

- Huszar et al modeled the climate impact due to aviation in 2013 [27] using the Météo-France CNRM-CM5.1 earth system model. Supercomputing at a remote location was however necessary to conduct the simulation, which imposes a major deficit compared to AirClim, which can be operated from any modern personal computer.
- Several studies of climate impact from aviation have used the U.S. Federal Aviation Administrations (FAA) Aviation Environmental Design Tool (AEDT). Unger et al [28] conducted research with similar uncertainty ranges, but used high performance computing centers for their simulations. On top of that, an AEDT license starts at 1200 USD.

A challenge in the field of climate assessment, is the metric to use when quantifying climate impact or climate change. In order to successfully reduce climate impact from aviation, climate impact needs to be quantified in such a way that it can be traced back to it's source. The quantification should be in such a way that the relevant climate agents can be compared on the same scale. This is a challenge due to the fact that the multiple climate species each have different lifetimes, with for example contrails dissipating in a matter of minutes to hours, and CO_2 being able to exist and remain in the atmosphere for decades.

A relevant and intuitive metric to measure climate change is the global mean surface temperature. The principle metric used for describing the contributions of the various effects is radiative forcing, which is measured in $\frac{W}{m^2}$. The temperature change ΔT_S (in K) can be computed with the following quasi-linear relation:

$$\Delta T_S \approx \lambda RF \tag{2.1}$$

In this relation, λ is the climate sensitivity parameter in $\frac{K}{Wm^{-2}}$ [12], which is a measure of how the global mean temperature changes due to a change in radiative forcing caused by an individual climate agent. The amount of temperature change that results from climate impact assessments, is highly dependent on the point in time that is considered. Therefore, a time-averaged temperature response metric is introduced; the Average Temperature Response, or ATR. The ATR can be computed by the following relation:

$$ATR_H = \frac{1}{H}\int_0^H \Delta T_S(t)dt \tag{2.2}$$

In this equation, H is the time horizon, which is the amount of years that is considered for averaging out the temperature response. The selection of the time horizon determines the relative difference of the species. A larger time horizon will generally provide a better representation of the long-lived species such as CO_2.

Alternative climate metrics have been used in past research. In 2013, the IPCC introduced the Effective Radiative Forcing (ERF) [29]. ERF quantifies the impact of climate agents that involve rapid adjustments to changes of components of the atmosphere and the surface. This feature makes ERF a better indicator than RF for aerosols and cloud changes.

In order to quantify the strengths of CO_2 and non-CO_2 radiative impacts, the IPCC introduced the Radiative Forcing Index (RFI) in 1999 [16]. The RFI is however not a CO_2 emission equivalence metric, as the computation of radiative forcing from CO_2 emissions is vastly different from non-CO_2 effects. CO_2 emissions cause long-term impact in the form of greenhouse gases while non-CO_2 emissions are short-term climate forcers. Due to the long lifetime of CO_2 in the atmosphere, it is necessary to include the complete history of emissions over time, while the non-CO_2 impact can be computed from the emission data of one year only.

The Global Warming Potential (GWP) was introduced at the Fifth Assessment Report in 2014 [29] to be a means of comparing the impact of the different climate agents. It is a measure of how much energy the emissions of 1 ton of a gas will absorb over a given period of time, relative to the emission of 1 ton of carbon dioxide. The downside of this metric lies in the fact that a timescale is required. Generally, a timescale is chosen at 100 years, which imposes an underestimation of CO_2 impact because the long lived effects are 'cut-off' after 100 years. Freeman et al [30] concluded in 2018 that using the GWP may incorrectly predict climate impact reductions due to these underestimations.

Fuglestvedt et al [31] considered near surface temperature changes as result of the various climate effects to be a suitable measure to compare the different climate agents, as it contains an artificial memory of the effects which enable comparison between long-term and short-term effects. Alternatively, Allen et al [32] have developed an adjusted, so-called"termed", Global Warming Potential (GWP*). This metric relates cumulative CO_2 emissions to short lived climate pollutants allowing accurate indications of the impact of both long-lived and short-lived species.

2.4. PERFORMANCE AND EMISSION MODELING

For accurate climate modeling of air traffic, it is a necessity to know the location, time, amount and composition of the emission. When merging these 4 aspects together, this becomes an emission inventory. This is similar to a conventional mission profile (a segmented flight trajectory in time and space), but with the addition of emission data. The amount and composition of the emission are determined by the aerodynamic and propulsive performance of an aircraft. The performance of an aircraft therefore needs to be modeled in order to predict the amount of fuel burn and how the composition of the emission will be.

Two existing performance models have been considered to use or take inspiration from: Base of Aircraft Data (BADA) from Eurocontrol [33] and OpenAP, developed at Delft University of Technology by J. Sun [34]. Both performance models work in a similar way, but OpenAP is currently considered the best option to use as the model is open-source and license-free. This enables making adjustments to be able to model a future aircraft such as the Flying V. More details on how OpenAP has been used is explained in section 3.1.

2.5. FLYING V

Last, the preliminary design of the Flying V was investigated. The design is discussed in section 2.5.1, while section 2.5.2 presents the opportunities and challenges that come with this novel configuration. Finally, section 2.5.3 elaborates on the recent developments in the Flying V project.

2.5.1. DESIGN

The Flying V aircraft is a high potential candidate of an alternative configuration. Like the name suggests, the Flying V is a V-shaped aircraft that no longer contains a conventional fuselage, but merges two fuselage sections with the left- and right wing. It is a tailless aircraft with two cylindrical pressured cabins placed in the leading edge of the flying wing and contains two over-the-wing engines. Figure 2.6 shows the original concept configuration from Benad [7]. Longitudinal and lateral control is provided by elevons. The wingtips carry out an additional role as vertical tail to provide directional stability. The mission of the Flying V is similar to the mission of the Airbus A350. It is able to transport 315 passengers and 160 m^3 of freight. The span of the aircraft is equal to that of the A350, enabling the usage of the same airport infrastructure.

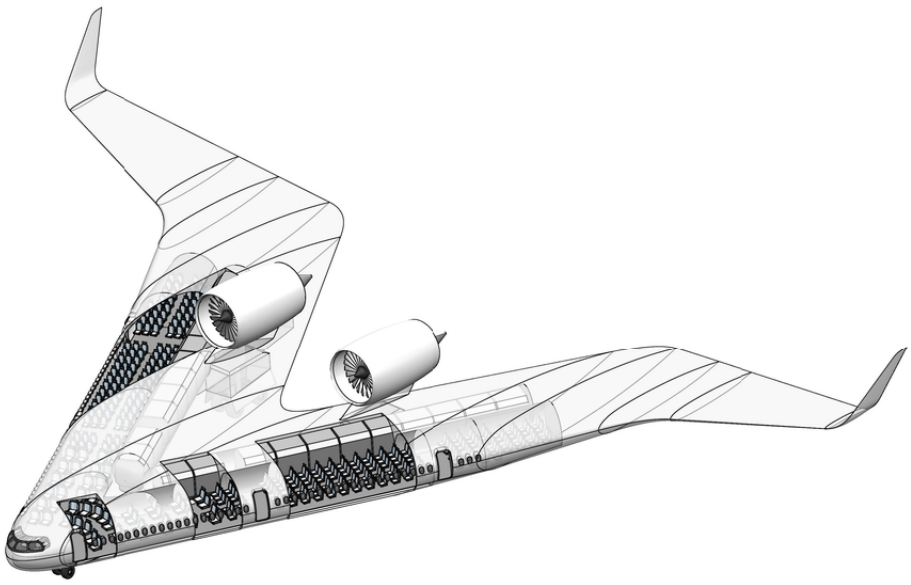

Figure 2.6: Flying V configuration [7]

2.5.2. OPPORTUNITIES AND CHALLENGES

The Flying V is a type of flying wing concept, which has two major benefits compared to a conventional tube-and-wing aircraft. First, the aerodynamic efficiency is superior due to the lower wetted area and lower interference drag of the concept. Secondly, having passengers and freight as well as fuel embedded in the wing structure allows for spanwise weight distribution [35], yielding a lower structural weight of the aircraft compared to conventional tube-and-wing aircraft.

Though the flying wing concept has been researched for over a century, it is still considered an unconventional configuration. A number of challenges have prevented the development of implementing this configuration in a passenger transport aircraft.

The first challenge is related to stability and control issues. Flying wings lack conventional stabilizing surfaces from a tail, which makes the aircraft unstable and difficult to control. Countermeasures to cope with these issues generally lead to an increase of weight and drag. Secondly, the cabin of a flying wing is generally not cylindrical, making it more difficult to pressurize. This results in a weight penalty. Lastly the flying wing concept imposes a compromise from the passenger's comfort. Outboard seated passengers are located further away from the center-line of the aircraft, making gusts and maneuvers less comfortable. Also, flying wing aircraft generally need a higher angle of attack during takeoff and landing, which is less comfortable for the passenger [35].

2.5.3. PROJECT DEVELOPMENT

Since the original design in 2015, several details of the concept have been researched into more detail. Amongst others, this includes research to the handling qualities (Cappuyns in 2019 [36]), landing gear implementation (Bourget in 2020 [37]) and engine integration (Empelen in 2020 [38]).

As of 2020, a family of Flying V aircraft are under consideration. Hillen in 2020 [39] and Oosterom in 2021

[40] have initiated the possibility for -800, -900 and -1000 variants of the Flying V to serve a wider range of airline requirements. For this research, the -900 variant is considered and compared to the -900 variant of the Airbus A350 family.

3

METHODOLOGY

This chapter contains the details of the methods used to provide results that can aid in answering the research questions from the previous chapter. The objective of the methodology is to have the ability to compute climate impact in terms of temperature change due to emissions of the A350-900 and the Flying V-900. An outlined overview of the methodology is presented in fig. 3.1. A city-pair can be entered into the routing network module along with a manually selected altitude, Mach number and aircraft type. The routing network module constructs a 3D flight trajectory. The performance module computes the fuel burn of a given flight trajectory and the flight planning module can construct an emission inventory by combining the 3D flight trajectory and fuel burn data. This emission inventory acts as an input for the climate assessment module, which finally computes the climate impact.

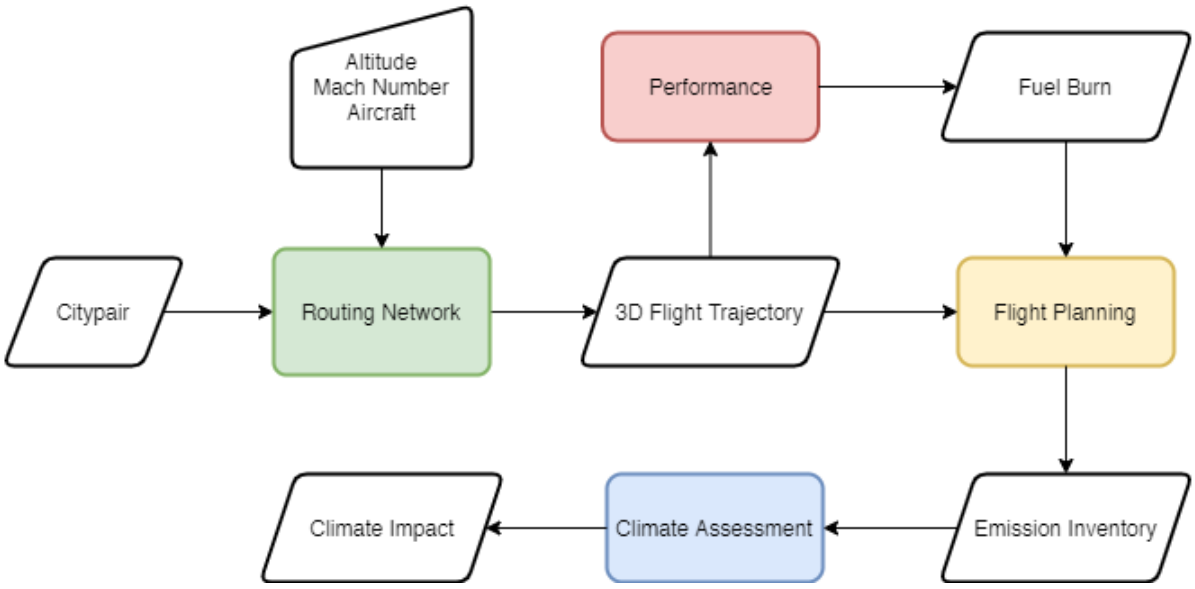

Figure 3.1: Methodology flowchart

The aforementioned 4 modules are addressed in the following sections:

- Performance (section 3.1)
- Routing network (section 3.2)
- Flight Planning (section 3.3)
- Climate Assessment (section 3.4)

The explanation of the modules will be supported by flowcharts, that contain the legend shown in fig. 3.2. Finally, section 3.5 will discuss how the aforementioned models work collectively to produce the required results.

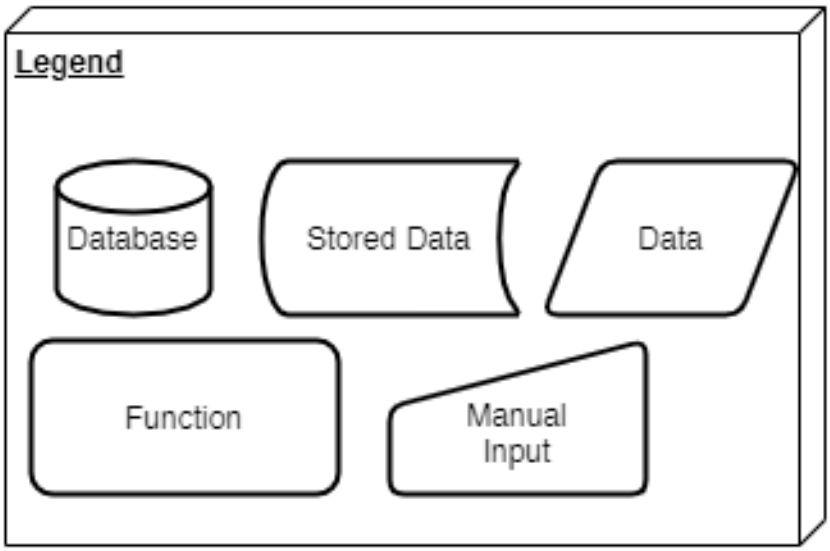

Figure 3.2: Legend of module flowcharts

3.1. PERFORMANCE MODELING

The performance of both aircraft is modeled by computing the required amount of fuel mass flow at specified operating conditions. In fig. 3.3, a visualisation of the inputs and outputs of the performance model is present. The fuel burn function is built in a Python environment.

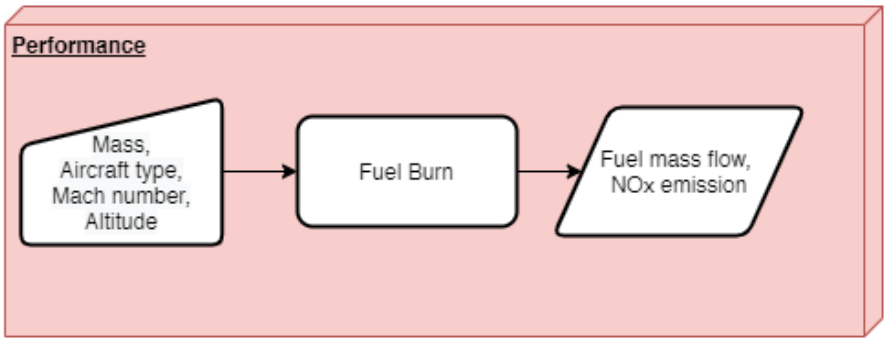

Figure 3.3: Performance model block

At given operating conditions, Mach number M, altitude h, mass m and flight path angle γ, both aircraft are required to produce lift and thrust for that particular flight condition. Section 3.1.1 discusses the aerodynamic performance. Here, the drag computation in operating conditions will be discussed. While section 3.1.2 discusses the propulsive performance. Section 3.1.3 describes how the performance model was verified.

3.1.1. AERODYNAMIC PERFORMANCE

In cruise conditions, the lift of the aircraft is considered equal to the aircraft weight. The weight of the aircraft is subdivided into 4 components:

- Operational Empty Weight (OEW)
- Payload Weight (PW)
- Reserve Fuel Weight (RFW)

- Fuel Weight (FW)

The OEW, PW and RFW are considered constant. The Fuel Weight is variable during a cruise segment. It starts at a certain value that depending on the required flight range and decreases as fuel is being burned during the mission. An overview of the values of the weights is given in table 3.1. Note that the payload weight is based on 315 passengers with baggage weighing 95 kg each. The listed fuel weight is at mid-cruise conditions at the design mission cruise range of 14800 km. The mid-cruise weight used for computing the optimum flight altitude later in this chapter. Finally, the reserve fuel weight is assumed at 5% of the maximum fuel weight. This parameter has been estimated roughly due to it's limited significance to the performance. The total weight W is computed by multiplying the total mass with the gravitational constant g.

Table 3.1: Component weights of A350-900 and Flying V-900

Component	A350-900	Flying V-900
OEW [kg]	142400	120000
PW [kg]	29925	29925
FW [kg]	48852	39646
RFW [kg]	5059	4630
Total mass [kg]	**223236**	**194201**

The aircraft weight W is set equal to the lift L (when assuming straight, symmetric flight) and then the required lift coefficient C_L can be determined by eq. (3.1):

$$C_L = \frac{L}{\frac{1}{2}\rho V_{TAS}^2 S_{ref}} \tag{3.1}$$

In this equation, ρ is the air density, which is dependent on altitude. In this model, an International Standard Atmosphere is assumed. Furthermore, V_{TAS} is the true airspeed and S is the reference wing area of either aircraft. The drag D of the aircraft can subsequently be obtained by eq. (3.2).

$$D = C_D \frac{1}{2}\rho V_{TAS}^2 S_{ref} \tag{3.2}$$

Here, C_D is the drag coefficient, which is determined by the drag polar. as discussed in the following section.

DRAG POLAR

The drag coefficient consists of a lift-dependent and a lift-independent component, otherwise known as the lift induced drag and the zero-lift drag. The drag polar is then described as:

$$C_D = C_{D0} + kC_L^2 \tag{3.3}$$

In eq. (3.3), C_{D0} is the zero-lift drag coefficient, and k is the lift-induced drag coefficient factor, respectively. The zero-lift drag coefficient is expressed as:

$$C_{D0} = C_f \frac{S_{wet}}{S_{ref}} \tag{3.4}$$

In this equation, C_f is the skin friction coefficient, while S_{wet} is the wetted area of the aircraft. The wetted area can be either computed analytically or taken from credible sources. The value for C_f can be read from fig. 3.5.

For the A350-900, the wetted area is obtained by calculating the area of the different components (wing, fuselage, vertical tail, horizontal, nacelles & pylons). Relations for the computing the wetted areas for the wing, tail and fuselage are taken from appendix A in Torenbeek (2013) [41]. The nacelle and pylon wetted areas are calcuated from equations in Synthesis of Subsonic Airplane Design by Torenbeek (1988).

Computation of the wetted area can be obtained in appendix A. For verification, the external cleaning areas as stated in Airport and Maintenance Planning report on the A350 from Airbus [42] have been used. Both the wetted areas calculated and found in literature are listed in Table 3.2 for each component.
For the Flying V-900, the wetted area is taken from the thesis report of Oosterom (2020) [40], where the wetted area was determined by a CAD kernel (ParaPy).

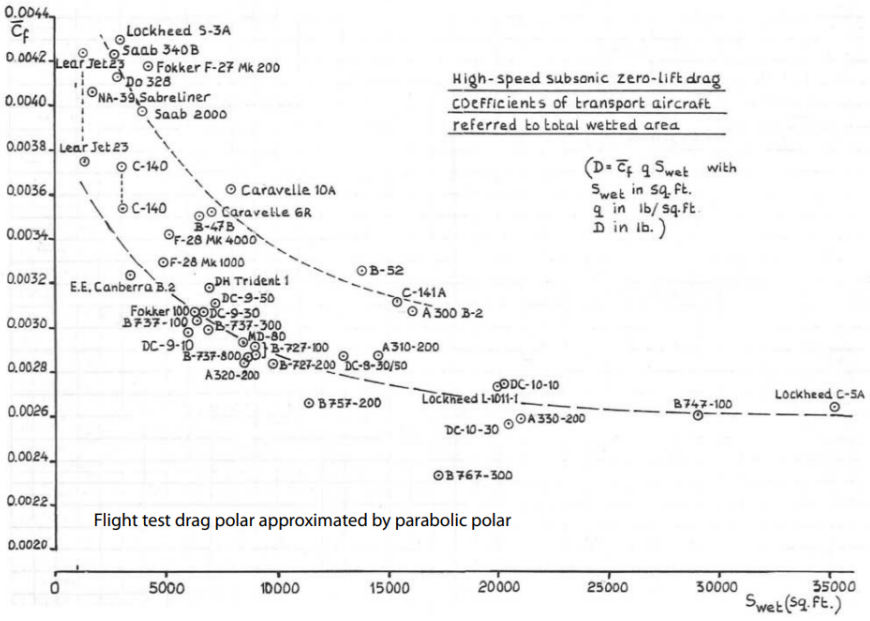

Figure 3.4: High-speed subsonic zero-lift drag of transport aircraft referred to total wetted area[8]

Table 3.2: Wetted Area A350-900 Components

Component	**Calculated S_{wet} [m^2]**	**$S_{cleaning}$ [m^2]**
Wing	777	763
Fuselage	1087	1073
Vertical Tail	104	102
Horizontal Tail	170	144
Nacelles & Pylons	178	166
Total	**2316**	**2248**

In eq. (3.3), k is dependent on the wing aspect ratio A_{ref} and the Oswald factor e as expressed in eq. (3.5).

$$k = \frac{1}{\pi A_{ref} e} \tag{3.5}$$

A_{ref} can be determined by eq. (3.6), where b_{ref} represents the wingspan. e can be determined from fig. 3.5.

$$A_{ref} = \frac{b_{ref}^2}{S_{ref}} \tag{3.6}$$

The above method however is considered insufficient due to the presence of winglets. Winglets change the effective span of a wing, therefore affecting the Aspect Ratio and Oswald factor. The effective wingspan b_{eff} is calculated as follows:

$$b_{eff} = b_{ref} + \frac{l_{winglet}}{2} \tag{3.7}$$

In this equation, $l_{winglet}$ is the winglet length. Together the reference Oswald factor e_{ref}, the effective Oswald factor can be computed with the following formula:

$$e_{eff} = e_{ref} \frac{b_{eff}}{b_{ref}} \tag{3.8}$$

The resulting relation describing the effective lift induced drag coefficient factor k_{eff} now becomes:

$$k_{eff} = \frac{1}{\pi A_{ref} e_{eff}} \tag{3.9}$$

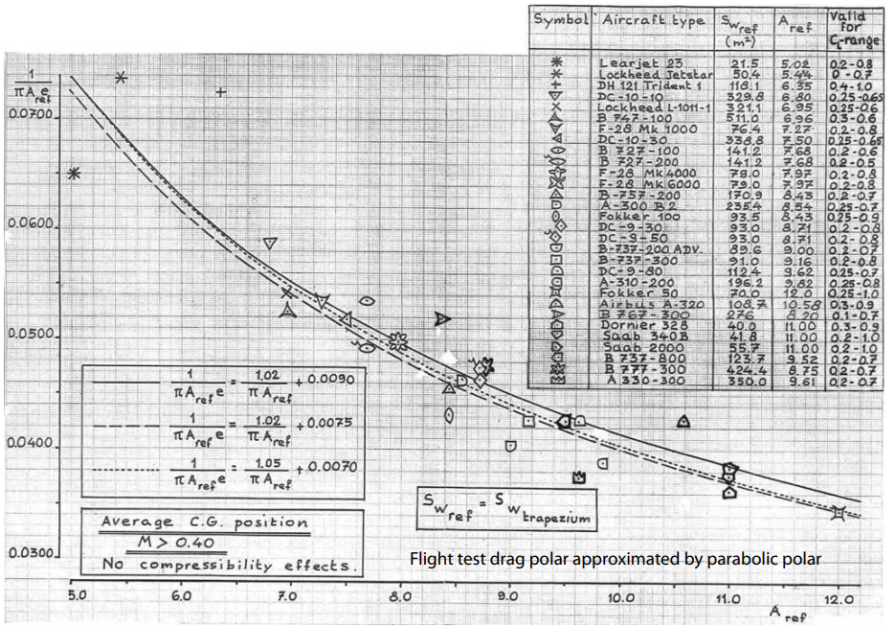

Figure 3.5: High-speed subsonic lift-dependent drag coefficient of transport aircraft [8]

Section 3.1.1 shows the values of parameters discussed in this section. The resulting drag polar data for both the A350-900 and Flying V-900 are presented in table 3.4

Table 3.3: Drag polar parameter values

Aircraft	C_f	b_{ref}	S_{ref}	A_{ref}	e_{ref}	b_{eff}	e_{eff}
A350-900	0.0265	64.8 m	442 m^2	9.49	0.78	65.6 m	0.79
Flying V-900	0.0268	60.8 m	860 m^2	4.30	0.88	64.9 m	0.92

Table 3.4: Drag polar data A350-900 and Flying V-900

Aircraft	C_{D0}	k
A350-900	0.0135	0.0424
Flying V-900	0.00644	0.0843

3.1.2. PROPULSIVE PERFORMANCE

At given flight conditions, a particular amount of thrust required by the two Rolls Royce Trent XWB-84 engines on both aircraft to overcome the drag and to be able to climb. The required thrust per engine is defined by the following equation, where n_{eng} is the number of engines.

$$T = \frac{(D + W \sin\gamma)}{n_{eng}} \tag{3.10}$$

The amount of fuel mass flow that is needed to produce a particular amount of thrust depends on the engine characteristics, and the operating conditions. First, the fuel mass flow to produce a particular thrust at sea level is determined.

STATIC FUEL MASS FLOW

For sea level thrust, a 3rd degree polynomial is used to interpolate the fuel mass flow response of the engines at 4 different thrust settings:

- Take-off (100%) - 2.819 $\frac{kg}{s}$

- Climb-out (85%) - 2.306 $\frac{kg}{s}$
- Approach (30%) - 0.801 $\frac{kg}{s}$
- Idle (7%) - 0.291 $\frac{kg}{s}$

The values for the ratings above have been obtained from the ICAO Emissions Data-Bank [43]. The polynomial in eq. (3.11) is fitted to the four datapoints. The result is shown in fig. 3.6.

$$ff_{sl} = C_{ff3}\frac{T}{T_0}^3 + C_{ff2}\frac{T}{T_0}^2 + C_{ff1}\frac{T}{T_0} \tag{3.11}$$

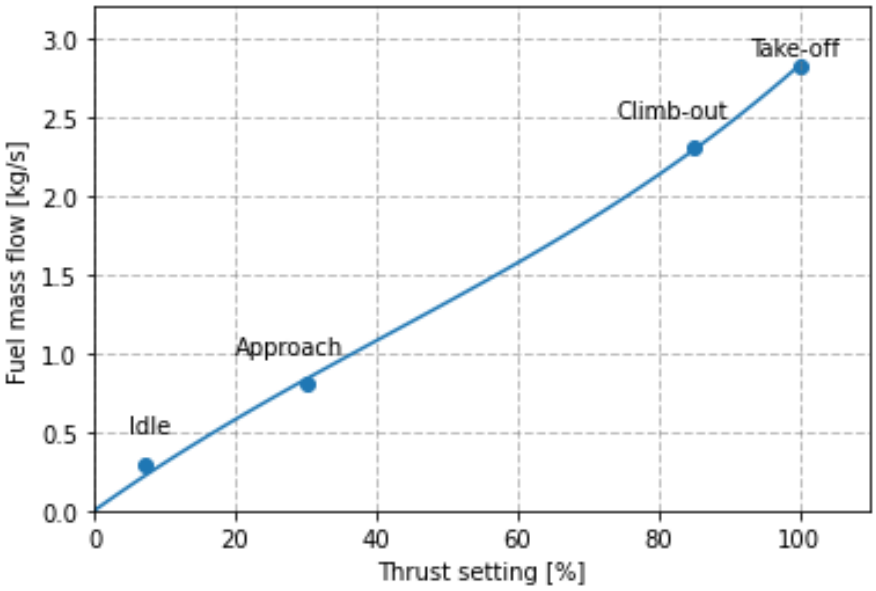

Figure 3.6: Interpolation of fuel mass flow curve

$\frac{T}{T_0}$ is the engine thrust setting. T is the required thrust and T_0 represents the maximum thrust of a particular engine, which is 379 kN for the Trent XWB-84. The resulting coefficient values are as follows:

- $C_{ff3} = 1.498$
- $C_{ff2} = -1.879$
- $C_{ff1} = 3.209$

When the coefficient- and maximum thrust values are incorporated into eq. (3.11), a fully functional relation between thrust and fuel mass flow is established. The next section will elaborate on the incorporation of altitude effects, i.e. the dynamic fuel mass flow.

DYNAMIC FUEL MASS FLOW

In 2020, J. Sun [34] developed an open-source fuel consumption model called OpenAP, which has similar functionalities as for example BADA [33]. OpenAP uses a linear relationship between altitude and fuel flow, where a correction factor, $C_{ff,ch}$ comes in.
This correction factor can either be computed with eq. (3.12) if the specific fuel consumption values at cruise level (SFC_{CR}) and sea level (SFC_{SL}) are known as well as the design cruise altitude for a specific engine (h_{CR}). Otherwise, an average value of $6.7 \cdot 10^{-7}$ is used.

$$C_{ff,ch} = \frac{SFC_{CR} - SFC_{SL}}{h_{CR}} \tag{3.12}$$

This correction factor can be implemented into the following relation to obtain a dynamic fuel mass flow formula as function of thrust:

$$ff_{sl} = C_{ff3}\left(\frac{T}{T_0}\right)^3 + C_{ff2}\left(\frac{T}{T_0}\right)^2 + C_{ff1}\left(\frac{T}{T_0}\right) + C_{ff,ch} \cdot T \cdot h \tag{3.13}$$

NO_x EMISSION

With a function to compute the fuel mass flow, it is also possible to predict the NO_x emission at given operating conditions. For NO_x prediction, the Boeing Fuel Flow Method 2 (BFFM2) is used [44]. The BFFM2 uses aircraft engine emission data available in the ICAO emissions databank. This database contains, just like fuel flow, emissions of NO_x, CO and HydroCarbons at the 4 aforementioned thrust settings. Interpolation is performed in between the 4 settings to relate the emissions to a specific thrust setting for the entire thrust spectrum.

Next, the BFFM2 imposes upscaling of the emissions to account for the differences in temperature, pressure and humidity at flight conditions compared to sea level conditions. The ratios for temperature (θ) and pressure (δ) are obtained from eq. (3.14) and eq. (3.16), respectively. These two ratios act as upscaling factors from reference (sea level) to non-reference (ambient) conditions.

$$\theta = \frac{\frac{T(h)}{288.15}}{\beta} \tag{3.14}$$

T is the ambient temperature in K, which is a function of altitude h. The Mach number correction factor β is obtained from:

$$\beta = \exp\left[0.2M^2\right] \tag{3.15}$$

In eq. (3.15), M is the Mach number.

$$\delta = \frac{\left(1 - \frac{0.0019812h}{288.15}\right)^{5.255876}}{\beta^{3.5}} \tag{3.16}$$

Next, the ratio of temperature and altitude from reference to ambient conditions is obtained from:

$$r = \frac{\theta^{3.3}}{\delta^{1.02}} \tag{3.17}$$

Now, for a given fuel flow rate ff_{AC}, the NO_x Emission Index (EINOx) can be calculated. First, the fuel flow at sea level (ff_{SL}) is obtained:

$$ff_{sl} = \frac{\frac{ff_{AC}}{n_{eng}}\theta^{3.8}}{\delta\beta} \tag{3.18}$$

In eq. (3.18), n_{eng} is the number of engines. Next, the NO_x emission index at sealevel $EINOx_{SL}$ is computed:

$$\mathrm{EINOx_{SL}} = 14.0253 ff_{SL}^{1.11045} \tag{3.19}$$

The specific humidity ω can be obtained from the following relation with altitude h:

$$\omega = 10^{-3}\exp[-0.0001426(h - 12900)] \tag{3.20}$$

Finally, the NO_x emission index at flight level $EINOx_{FL}$ can be obtained:

$$\mathrm{EINOx_{FL}} = \mathrm{EINOx_{SL}}\sqrt{\frac{1}{r}}\exp\left[-19(\omega - 0.00634)\right] \tag{3.21}$$

With the above expression, the performance model is complete in the sense that it can compute the fuel mass flow and the NO_x Emission Index for a given aircraft at specified operating conditions.

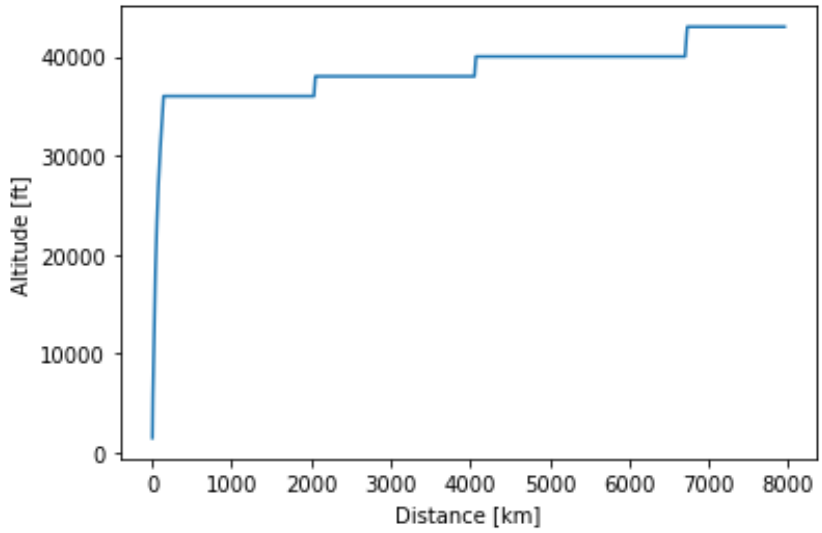

Figure 3.7: Mission profile verification

3.1.3. VERIFICATION

The performance model was verified by comparing the fuel mass flow and NO_x emission results with data from Piano-X for the A350-900 aircraft. A mission profile containing a climb segment and cruise segments at four different altitudes are considered. The mission profile in terms of horizontal distance and altitude is presented in fig. 3.7.

Over this mission profile, the fuel burn is computed and plotted against time. Also, the decreasing aircraft mass is plotted against time. The results from Piano-X and the performance model are presented in fig. 3.8.

It is evident that the performance model overestimates the fuel burn slightly over the entire mission, with an average error of 6.9%. It has been concluded that this is mainly caused by drag polar coefficient values that are a bit different in the Piano-X model. In order to see the results from both models with identical drag polar values, the drag polar from Piano-X is copied to the performance model, and the results are re-evaluated, which are documented in appendix E.

From the total values and errors documented in table 3.5, it is evident that the error in fuel flow computation becomes very small at identical drag polar values.

Table 3.5: Fuel burn and NO_x emission module vs. Piano-X

	Model (original)	**Model (modified)**	**Piano-X**	**Error (original)**	**Error (modified)**
Fuel Burn [kg]	98328	89875	90974	8.1%	1.2%
NO_x Emission [kg]	1733	1445	1571	10.3%	8.0%

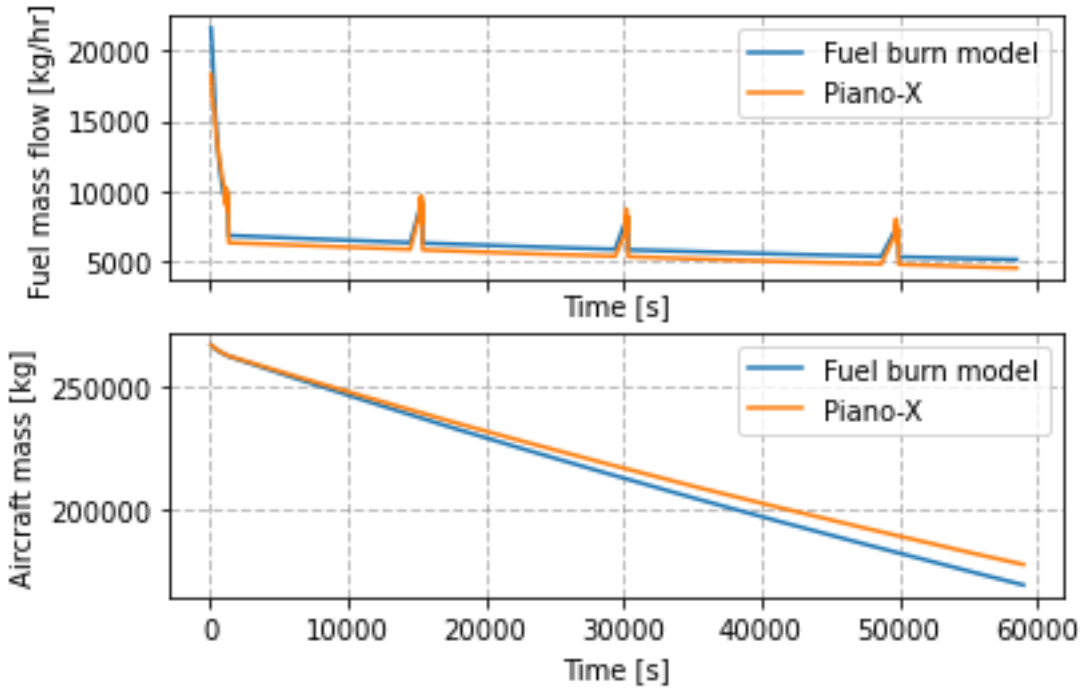

Figure 3.8: Verification performance model vs. Piano-X

3.2. ROUTING NETWORK

For modeling climate impact for a specific aircraft fleet, it is required to be able to accurately represent the routing network. This routing network can form part of the emission inventory, which is the input for the climate assessment module. For this, the routing network module is introduced. An overview of the model is presented in fig. 3.9. The model is decomposed into an airport database, a coordinates function and a trajectory function as discussed in section 3.2.1, section 3.2.2 and section 3.2.3, respectively.

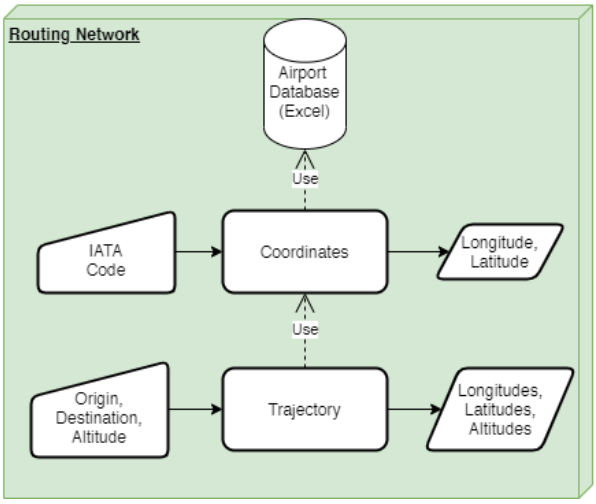

Figure 3.9: routing network module block

3.2.1. AIRPORT DATABASE

An airport database has been constructed in a Microsoft Excel sheet. The raw airport data is drawn from the openflights database[1]. The regional airports not containing IATA codes have been filtered out for convenience, with a total of 5287 airports remaining. For each airport, the following data are available:

- Name, e.g. *Amsterdam Airport Schiphol*
- City, e.g. *Amsterdam*
- Country, e.g. *Netherlands*
- IATA Code, e.g. *AMS*
- ICAO Code, e.g. *EHAM*
- Latitude, e.g. *52.3086°*
- Longitude, e.g. *4.76389°*
- Altitude, e.g. *-11 ft*

3.2.2. COORDINATES FUNCTION

A coordinates function has been constructed in a Python environment to be able to retrieve the location of an airport. The input of this function is the airport code in IATA format. The function looks up the code in the airport database and returns the longitude and latitude of the airport in degrees. For example, inputting "AMS" (IATA Code for Amsterdam Airport Schiphol), returns longitude 52.3086° and latitude 4.76389°.

[1] openflights.org/data.html

3.2.3. TRAJECTORY FUNCTION

With the ability to get the geographical locations of airports, it is possible to produce coordinate pairs for origins and destinations of specific flights. The flight route in between two airports can then be constructed via a Great Circle trajectory, which is what a civil aircraft would fly along in an idealized scenario to get from origin to destination.

The great circle trajectory is constructed with the Python geographiclib site package [2], which is able to calculate the distance between two sets of coordinates. It contains amongst others an Inverse solution to the geodesic equations, which enables the building of a Great Circle trajectory between two points on the globe via the GeodesicLine object.

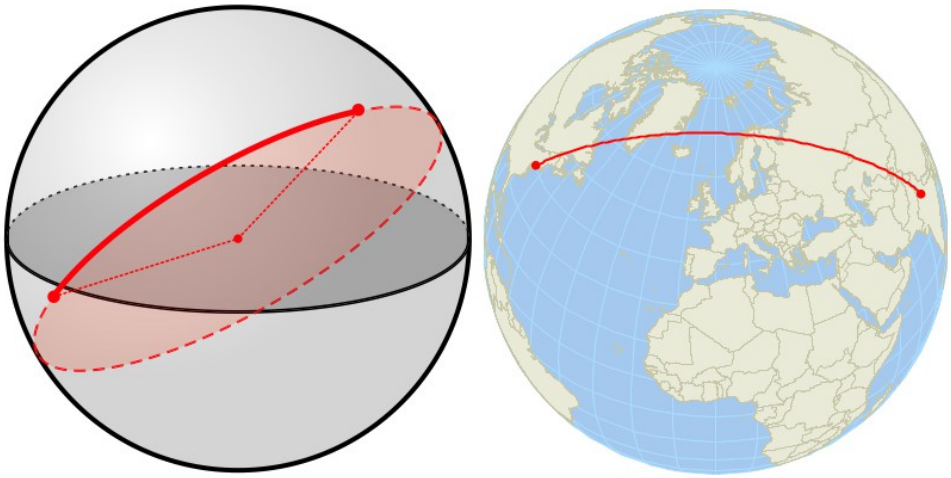

Figure 3.10: Great circle trajectory

The working principles of a great circle trajectory is expressed in fig. 3.10. The earth is assumed to be a perfect sphere. The shortest way from one point on a sphere to another is over a great circle. The great circle is constructed by drawing a circle with the center of the sphere as the circle's midpoint and crossing the origin and destination point. The length of the trajectory is equal to the arc length of the great circle section.
A result of this function be seen in fig. 3.11. It contains a sample of 4 arbitrary city-pairs:

- Amsterdam - Singapore
- San Francisco - Madrid
- Buenos Aires - Johannesburg
- Abu Dhabi - Melbourne

The trajectory function is written in Python with the time step dt as a variable, which is representative for the resolution of the trajectory. A smaller time step (e.g. 1 second) imposes a larger set of trajectory points then a larger time step (e.g. 60 seconds). The choice of which time step to pick is generally a trade-off between accuracy and computing time.

[2] https://geographiclib.sourceforge.io/1.50/python/

Figure 3.11: Great circle trajectory examples

3.3. FLIGHT PLANNING

With functions available for making aircraft routes between citypairs and calculating the fuel mass flow along the way, it is possible to construct a full emission inventory; a dataset of a particular set of flights burning fuel at specified locations along the globe. The aircraft fleet is discussed first in section 3.3.1 and the construction of the emission inventory is elaborated in section 3.3.2. An overview of the flight planning model is shown in fig. 3.12.

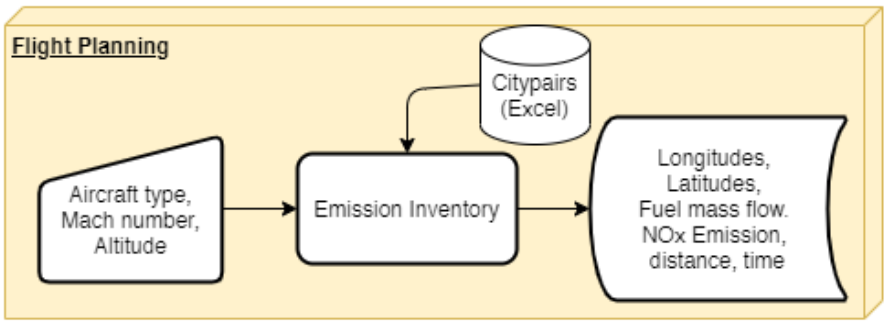

Figure 3.12: Flight planning model block

3.3.1. AIRCRAFT FLEET

The choice of which aircraft fleet to use for both aircraft is a rather complex trade-off. The A350-900 and the Flying V-900 are not at the same Technology Readiness Levels (TRLs). The A350 family has been operational as of 2013, while the Flying V family is still in an early development stage. The Flying V is proposed as a potential replacement aircraft for the A350. If an airline would want to be able to make the choice between buying one of the two aircraft, it is necessary to assess their relative performance and climate impact under the same circumstances. Therefore it is concluded relevant to compare a fleet of A350-900s with a replaced fleet of Flying V-900s.

In reality, the fleet development from A350's to Flying V's would be gradual, with replacements spread over a longer period of time. This is however rather hard to accurately predict and implement into the climate modelling methods. Therefore, an idealized fleet development scenario is considered where the entire fleet of A350 aircraft is replaced by Flying Vs at the same time in the year 2050.

To construct an A350 fleet which is as accurate and comprehensive as possible, a list of operators has been obtained. Per operator, the city-pairs that they serve are listed and summarized in a small database [3]. The complete set of flights is documented in appendix B. The flight network corresponding to these city-pairs is summarized in fig. 3.13.

The market share of these A350 routes is expressed RPK. When assuming that the 239 city-pairs in the A350 network operate twice per day (outbound and inbound) 365 days per year, the RPK becomes about 387 billion. The total RPK of the year 2019 was roughly 8686 billion, which enables roughly estimating the market share of the A350 fleet at about 4.5%.

3.3.2. EMISSION INVENTORY

With a determined aircraft network in terms of daily operating city-pairs, an aircraft emission inventory can be set up. The emission inventory is a required input for the AirClim software that is used in the climate model as discussed in section 3.4.1. The emission inventory consists of a set of 3D geographical locations with a corresponding amount of fuel burned, NO_x emitted, distance flown and exposure time. The emission inventory has a standard layout, with 7 columns:

- Longitude, fp_lon in ° East/West
- Latitude, fp_lat in ° North/South
- Pressure altitude, fp_alt in hPa
- Fuel burn, fp_fuel in kg

[3] https://www.airportspotting.com/airbus-a350-routes/

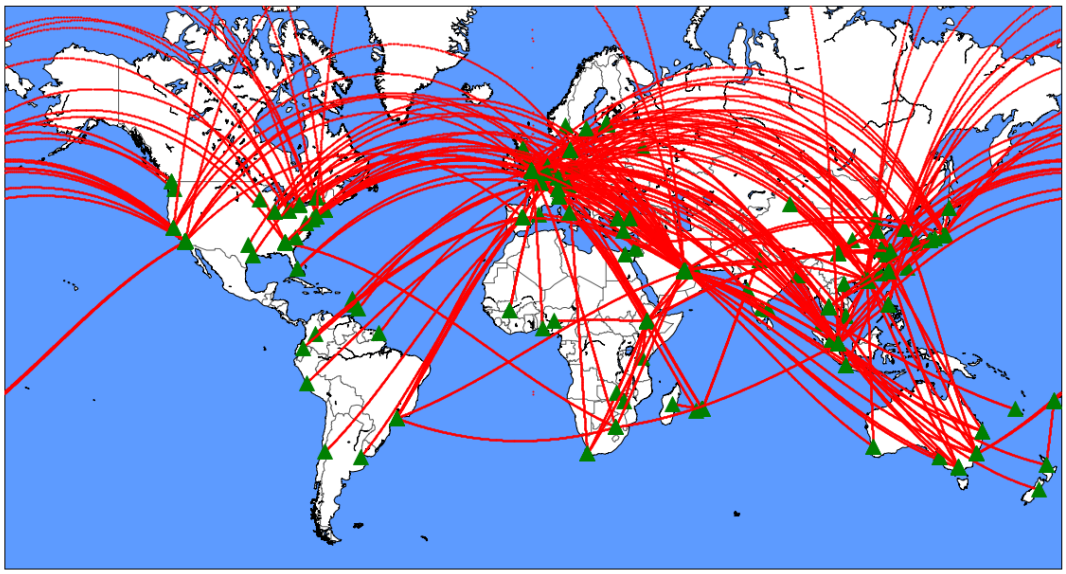

Figure 3.13: Global network of city-pairs A350

- NO_x emission, fp_nox in kg
- Distance, fp_dist in km
- Time frequency, fp_time in $\frac{1}{\text{year}}$

The columns longitude, latitude and pressure altitude are filled by the routing network module discussed in section 3.2. For each flight in the mentioned network, the trajectory function constructs a 3D flight, while assuming cruise phase only, from the origins to the destinations. The trajectories are then inputted to the performance model in order to compute the fuel mass flow and NO_x emission over the entire trajectory.
In order to account for sufficient fuel onboard for each flight, an iteration process is implemented for the fuel mass flow with the following scheme:

1. An initial guess of the amount of fuel required is made, based on the required cruise range R_{CR}:
   A350-900: $FM_{initial} = 8.75 \cdot R_{CR}$
   Flying V-900: $FM_{initial} = 6.35 \cdot R_{CR}$
2. The fuel burn and the NO_x emission for the full trajectory is calculated. The fuel mass FM decreases as the trajectory proceeds due to the burning of the fuel.
3. When the trajectory is fulfilled, the remaining amount of fuel (either a surplus or a shortage) is computed.
4. If there is a shortage of fuel to fulfill the mission, the shortage is added to $FM_{initial}$ and step 2 is triggered once more. If there is a surplus of fuel to fulfill the mission, the surplus is subtracted form $FM_{initial}$ and step 2 is triggered again.
5. The loop stops when the difference between the remaining amount of fuel becomes smaller than 1.0 kg.

Finally, the latter two columns are filled. The distance column is constructed by computing the amount of kilometers that are flown from one geographical location to another. The time frequency is by definition the amount of times that a trajectory segment with a particular time step occurs per year, which is generally twice per day, thus 730 times per year for daily operating city-pairs.

3.4. CLIMATE ASSESSMENT

With a working tool to construct emission inventories for given sets of flights at specified operating conditions, it is possible to simulate the climate impact of a particular emission scenario. The software used for

this is AirClim, which is discussed in section 3.4.1. In simulations of temperature response due to emissions, a number of uncertainties arise. In order to determine the margins of uncertainty, Monte Carlo simulations are performed, of which the details are discussed in section 3.4.2.

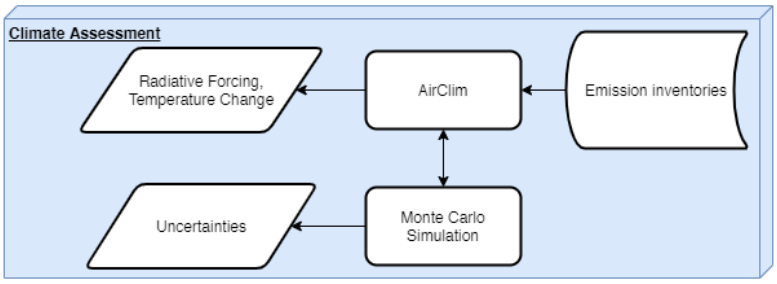

Figure 3.14: Climate model block

3.4.1. AIRCLIM

AirClim is a relatively modern climate impact simulation model developed by V. Grewe at the German Aerospace Center (DLR) [1]. This tool takes into account the effects of climate agents CO_2, NO_x, water vapour and exhaust contrails. The increased ozone production and decrease of methane lifetime and background ozone reduction are modeled following the quantification of NO_x emission.

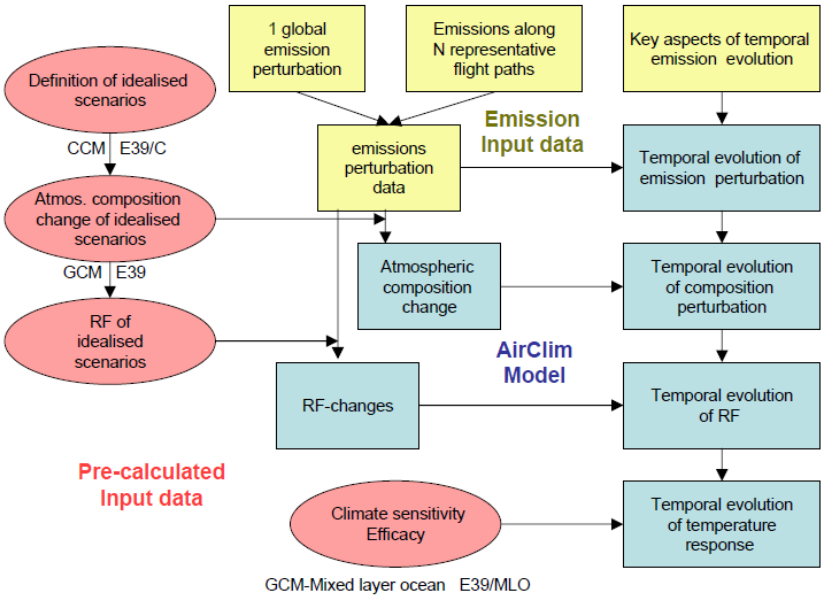

Figure 3.15: AirClim overview [1]

An overview of how AirClim operates can be seen in fig. 3.15. It takes pre-calculated atmospheric data obtained from a state-of-the-art climate chemistry model E39/C, developed by Hein et al [45]. 25 simulations with idealized emission scenarios have been performed with E39/C to create a data-set covering a wide range of emission scenarios. This data is combined with the perturbations from the emission data to compute atmospheric concentration changes and the resulting radiative forcing and near surface temperature changes.

3.4.2. MONTE CARLO SIMULATION

The outputs generated by the AirClim software, are dependent on assumptions of a number of parameters. The parameters that contain a range of uncertainty are:

- Stratospheric and tropospheric lifetimes τ_{strat} and τ_{trop}

- Climate sensitivity parameters λ of the 6 climate agents
- Lifetimes τ of the 6 climate agents

For each of these uncertainty parameters, 10,000 random samples are created. These samples have a uniform distribution between the lower and the upper limit of the uncertainty parameter. After compiling the AirClim software with the best estimates of the uncertainty parameters, the AirClim software is recompiled with 10,000 different compositions of uncertainty parameters. The results of these recompilations are stored for interpretation.

Uncertainty Parameter	Best estimate	Lower Limit	Upper Limit
τ_{strat}	1.0	0.6	1.4
τ_{trop}	1.0	0.8	1.2
λ_{CO2}	0.73	0.69	0.77
λ_{H2O}	0.83	0.58	1.08
λ_{O3}	1.00	0.70	1.30
λ_{CH4}	0.86	0.77	0.95
λ_{PMO}	1.00	0.70	1.30
λ_{Cont}	0.43	0.39	0.47
τ_{CO2}	1.00	0.95	1.05
τ_{H2O}	1.00	0.5	1.5
τ_{O3}	1.00	0.5	1.5
τ_{CH4}	1.00	0.9	1.1
τ_{PMO}	1.00	0.5	1.5
τ_{Cont}	1.00	0.5	1.5

Table 3.6: Uncertainty parameters

3.5. SYNTHESIS

Figure 3.16 shows the full set of model blocks and how they work together. The Climate Impact model uses the Flight Planning model to create an emission inventory. This emission inventory is built by using the routing network module to create three-dimensional trajectories and by using the Performance model to compute the corresponding fuel burn and NO_x emission in the trajectories.

The complete architecture is controlled by a Python script that calls the various models when needed. With the exception of AirClim and the Monte Carlo Simulations, all of the models are written as functions in Python. The airport database and the set of flight routes containing city-pairs are necessary Microsoft Excel sheets for running the architecture.

Furthermore, AirClim and the Monte Carlo Simulations need to be run from a Linux environment. This Linux environment is set up such in Python that it can be controlled from a windows environment as well. To be able to do this, the user of the software should have some form of Linux terminal available on his or her personal computer. This can either be on standard Linux software such as Ubuntu, but also from a Linux Bash Shell application available for Windows. FORTRAN should be installed on the operating system, as well as the subprocess site package for Python.

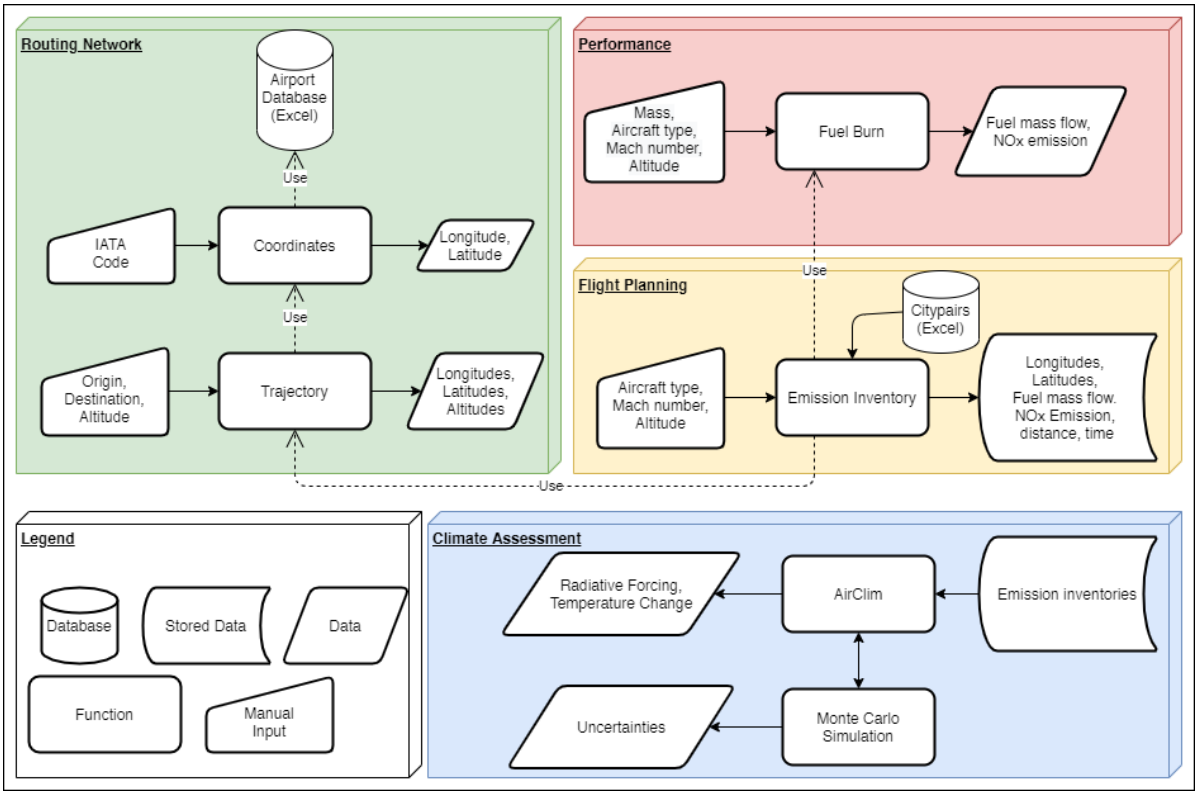

Figure 3.16: Model architecture

4

RESULTS

This chapter elaborates on the results produced during the course of this research. In section 4.1, the comparison between the A350-900 and the Flying V-900 will be discussed at design conditions. Next, a sensitivity analysis is described in section 4.2 and the uncertainty ranges are determined in section 4.3. Finally, section 4.4, will elaborate on the optimization study performed to find the optimum operating conditions for minimum climate impact.

4.1. DESIGN CONDITIONS COMPARISON

First, the comparison between the two aircraft was done at design operating conditions. The design cruise mach number for both aircraft is 0.85. The optimum altitude is however to be determined. From a performance perspective, it is considered that the optimum altitude is that at which fuel consumption is minimal. Section 4.1.1 will show the comparison from a performance perspective. Later on, section 4.1.3 will compare the aircraft from a climate impact perspective.

4.1.1. OPTIMUM ALTITUDE

From a purely aerodynamic perspective, the optimum cruise altitude would be where the Lift-to-Drag ratio $\frac{L}{D}$ is largest. For both aircraft, the $\frac{L}{D}$ is plotted against altitude to find their respective optima in fig. 4.1. For the A350-900, the maximum $\frac{L}{D}$ is 20.9 at at 12 699 m, while the Flying V-900 maximum $\frac{L}{D}$ is 21.4 at an altitude of 13 258 m. It is distinguished from fig. 4.1 that the Flying V-900 outperforms the A350-900 in terms of aerodynamics at altitudes above 11000 m. Below that, the difference between the two is in favour of the A350-900.

In addition to the $\frac{L}{D}$, the weight of the aircraft is a factor influencing it's aerodynamic performance. A lower weight leads to a lower drag according to the following equation:

$$D = \frac{C_D}{C_L} \cdot W \tag{4.1}$$

Figure 4.2 and fig. 4.3 show the lift and drag coefficients plotted against altitude for both aircraft. It is clear that the A350-900 operates at higher lift- and drag coefficients over the entire altitude spectrum.

Lower drag leads to lower thrust and thus lower fuel consumption. However, as discussed in section 3.1.2, propulsive performance can decrease at higher altitudes due to the altitude correction factor. Therefore, the fuel mass flow is also plotted against altitude for both aircraft in fig. 4.4

From a fuel performance perspective, the Flying V-900 outperforms the A350-900 on the entire altitude spectrum. However, it must be noted that the optimum altitudes are lower for minimum fuel flow, than for maximum $\frac{L}{D}$. This is further emphasized in fig. 4.5, fig. 4.6, fig. 4.7 and fig. 4.8: the optimum altitude is pushed downwards for both aircraft due to the altitude correction factor as explained in section 3.1.2.
For the A350-900, the optimum altitude then becomes 10 772 m, while the Flying V-900 optimal altitude becomes 11 424 m.

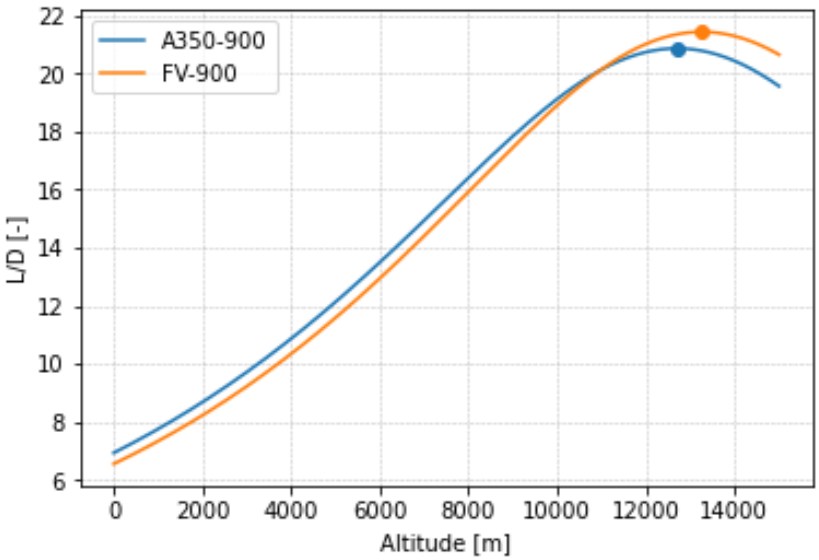

Figure 4.1: $\frac{L}{D}$ vs. altitude

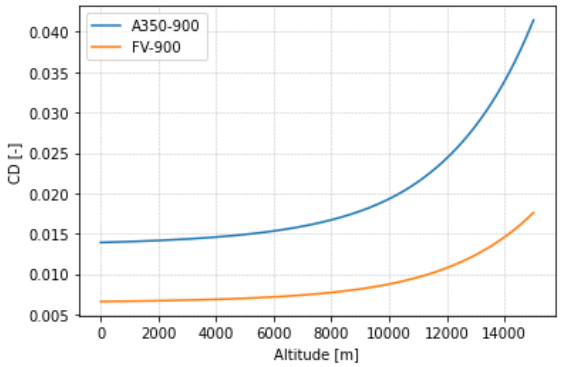

Figure 4.2: Drag coefficient vs. altitude

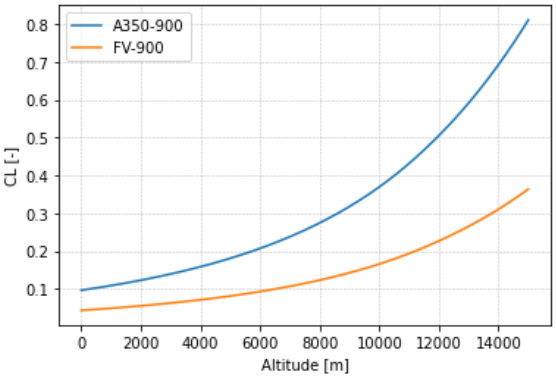

Figure 4.3: Lift coefficient vs. altitude

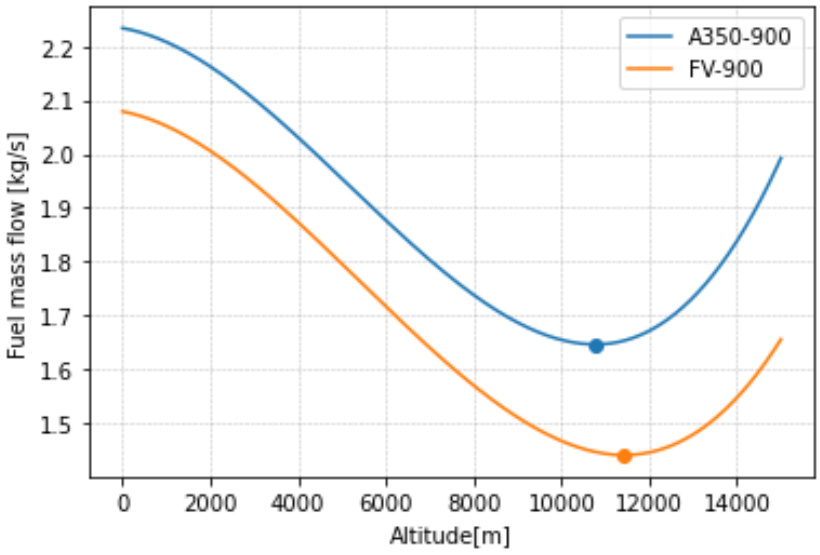

Figure 4.4: Fuel flow vs. altitude

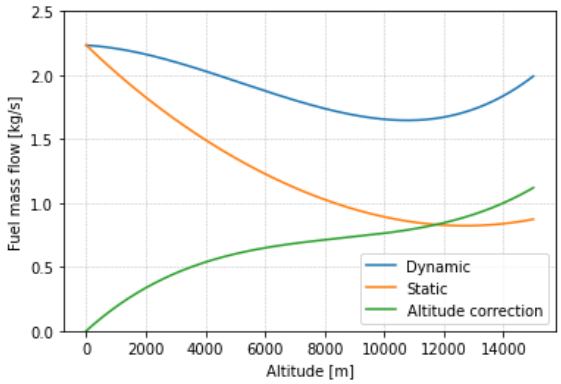

Figure 4.5: A350-900: Fuel flow vs. altitude

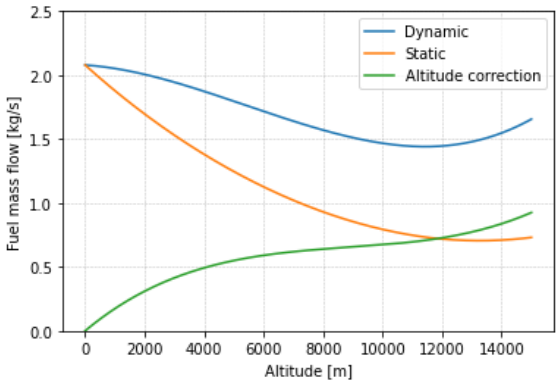

Figure 4.6: Flying V-900: Fuel flow vs. altitude

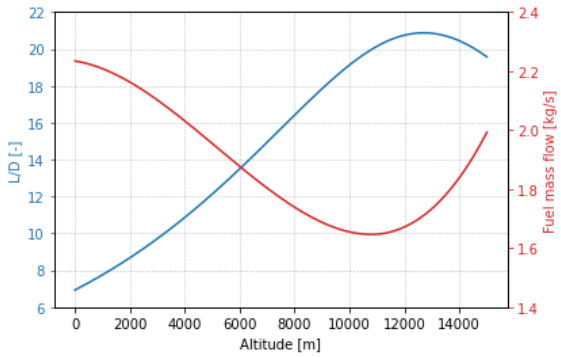

Figure 4.7: A350-900: $\frac{L}{D}$ and fuel flow vs. altitude

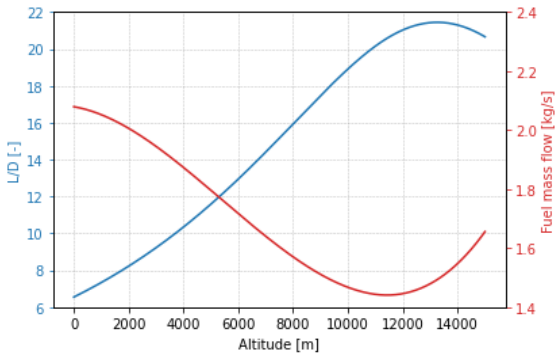

Figure 4.8: Flying V-900: $\frac{L}{D}$ and fuel flow vs. altitude

4.1.2. EMISSION INVENTORIES

For these optimum altitudes, emission inventories have been constructed for both aircraft. The full fleet as discussed in section 3.3.1 is considered. The the fuel efficiencies that follow from these emission inventories are as follows. The default scenarios for the CH_4-, CO_2- and fuel-backgrounds have been used.

- A350-900: 19.71 $\frac{g}{pax-km}$
- Flying V-900: 17.24 $\frac{g}{pax-km}$

The longitudinal and latitudinal distributions of the emission inventory are shown in fig. 4.9 and fig. 4.10.

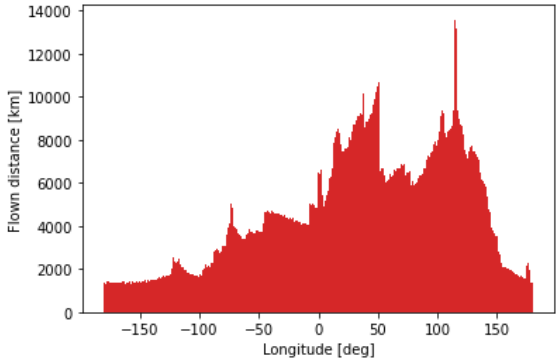

Figure 4.9: Longitudinal distribution of emission inventory

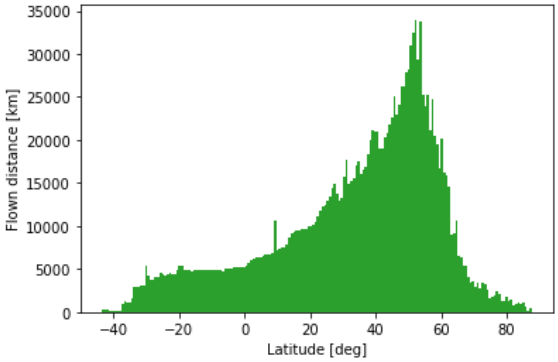

Figure 4.10: Latitudinal distribution of emission inventory

4.1.3. CLIMATE IMPACT

For the comparison in terms of climate impact, the near temperature change over time and the ATR are considered. The temperature change development over time due to the emissions from both aircraft can be seen in fig. 4.11 and fig. 4.12. It becomes clear that the differences between the temperature response of both aircraft is small.

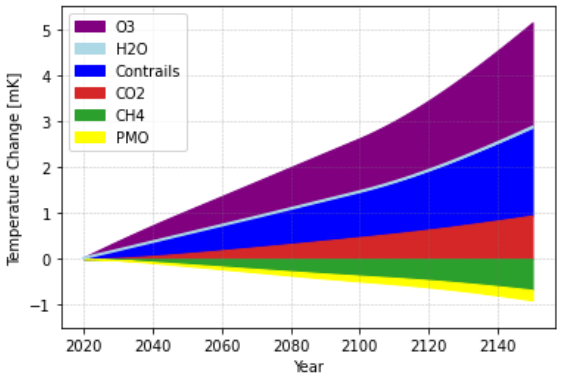

Figure 4.11: A350: Temperature change response

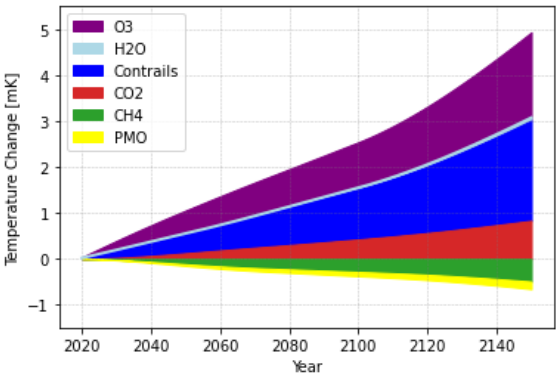

Figure 4.12: Flying V: Temperature change response

Looking at the average temperature response provides an easier way to emphasize differences in climate effects of both aircraft. Figure 4.13 shows in one image the differences between the two aircraft per climate agent in terms of ATR. The values of this figure are shown in table 4.1. The time horizon is set to 100 years. In general, it is preferred to have the time horizon as long as possible. The simulations in this research start in 2020 and applies the fleet replacement in 2050. The simulation ends in 2150, which makes 100 years the longest available time horizon to compare the two different fleet of aircraft.

The total ATR for the A350-900 is 2.29 mK, while it is 2.31 mK for the Flying V-900, yielding a difference of just 1%, but in favour of the A350-900. The reduced fuel burn of the Flying V causes a reduction in CO_2 and NO_x emission, leading to lower warming effects from direct CO_2 (10%), and O_3 (14%) and less cooling effect from CH_4 and PMO (both 22%, respectively). The Flying V however sees increased effects from H_2O (35%)

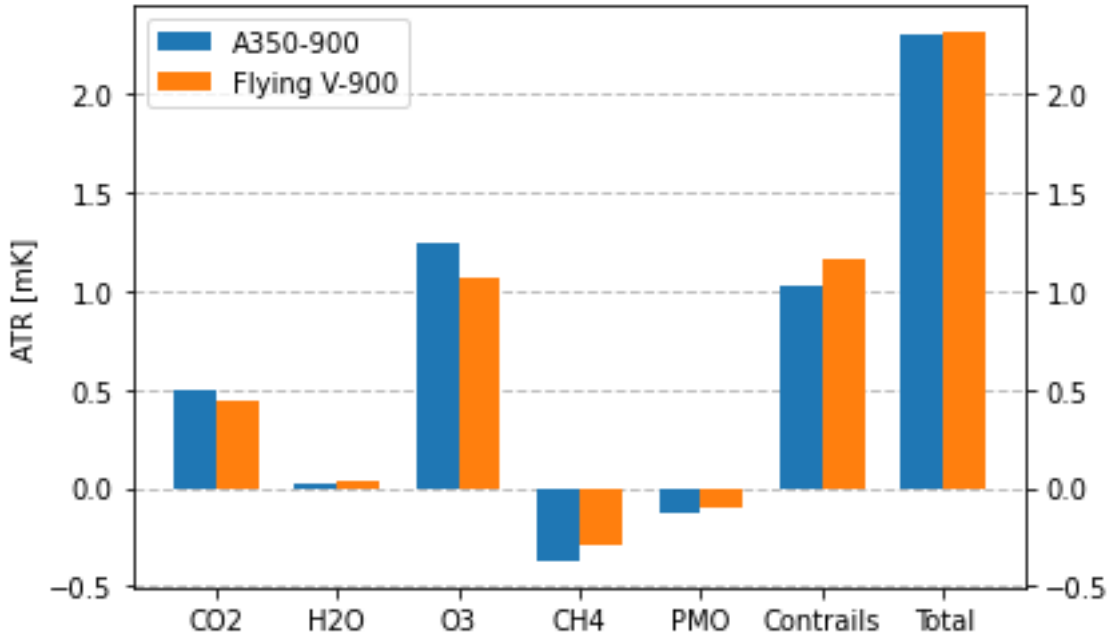

Figure 4.13: Bar chart A350-900 vs. Flying V-900

Table 4.1: ATR overview of climate agents A350-900 and Flying V-900

Climate Agent	**A350-900 ATR [mK]**	**Flying V-900 ATR [mK]**	**Difference**
CO_2	0.49	0.44	-10%
H_2O	0.02	0.03	35%
O_3	1.25	1.07	-14%
CH_4	-0.37	-0.29	-22%
PMO	-0.12	-0.10	-22%
Contrails	1.03	1.16	13%
Total	2.29	2.31	1%

and Contrails (13%), which is most likely due to the higher altitude at which the Flying V operates compared to the A350. In total, the difference between the two in terms of climate impact is effectively 1%.

To put these results into perspective, the total amount of anthropogenic climate change is considered. By 2050, mankind is expected to be responsible for a global temperature increase of 0.7 K [14]. Assuming 5% contribution from aviation yields a temperature increase of 35 mK from aviation. The fleet of A350 and Flying V aircraft would therefore be responsible for roughly 6.5% of the climate impact from aviation.

4.2. SENSITIVITY ANALYSIS

Next to the climate impact of the two aircraft in design conditions, it is also relevant to know how they perform when Flying in off-design conditions. Mach number and altitude analyses have therefore been performed, which are elaborated in section 4.2.1 and section 4.2.2, respectively. Later on, local effects are elaborated in section 4.2.3, where differences of climate agents at various latitudes are analyzed. Finally, section 4.2.4 and section 4.2.5 discuss the effects of using different backgrounds for Methane and Carbon Dioxide as well as different fuel scenarios.

4.2.1. MACH NUMBER EFFECTS

For investigating the effects of changing Mach number, cases have been selected:

1. $M = 0.87$
2. $M = 0.85$
3. $M = 0.825$
4. $M = 0.80$
5. $M = 0.775$

These cases have been inputted into the climate model, yielding the results per climate agent as shown in fig. 4.14 and fig. 4.15. The total results are documented in table 4.2 and table 4.3.

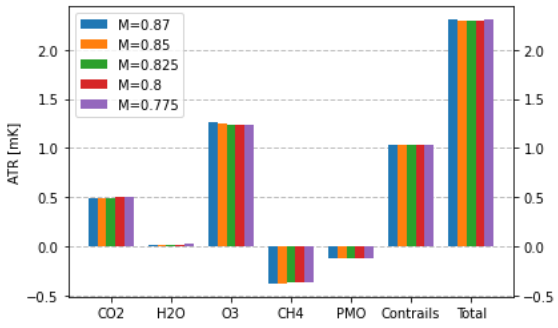

Figure 4.14: A350: Mach effects

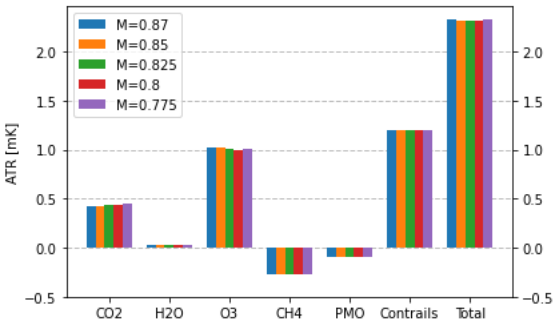

Figure 4.15: Flying V: Mach effects

Table 4.2: A350: effects of varying Mach number

Mach number	Fuel consumption [$\frac{g}{pax-km}$]	EI NO_x [g/kg]	ATR [mK]
0.87	19.58	14.59	2.30
0.85	19.71	14.84	2.30
0.825	19.90	15.17	2.29
0.8	20.22	15.56	2.29
0.775	20.59	15.92	2.30

Table 4.3: Flying V: effects of varying Mach number

Mach number	Fuel consumption [$\frac{g}{pax-km}$]	EI NO_x [g/kg]	ATR [mK]
0.87	17.13	13.17	2.32
0.85	17.24	13.38	2.32
0.825	17.45	13.66	2.31
0.8	17.71	14.01	2.32
0.775	18.09	14.32	2.33

The changes in climate impact due to changing Mach number are relatively small. There is an optimum mach number around $M = 0.825$, but the change when deviating from here is marginal. A note must be placed under these results. Namely that in general, slower aircraft have less climate impact. This is under the presumption that those aircraft are specifically designed for lower speed, which is not the case in this analysis. This analysis just considers changing from design to off-design operating conditions, without changing the physical design of the aircraft. Due to the constant altitude in this analysis, the impact from contrails and water vapour hardly change. CO_2 emission increases when flying slower, due to decreased aerodynamic performance. NO_x emission however decreases at slower speeds due to superior propulsive performance at lower thrust settings.

4.2.2. ALTITUDE EFFECTS

To determine the effects of changing altitude, 5 cases are analyzed for each aircraft; at 13, 12, 11, 10 and 9 km altitude. The results for each climate agent are analyzed individually. Overviews of the results of both aircraft are presented in fig. 4.16 and fig. 4.17. The temperature change development over time for each climate agent are available in appendix C.

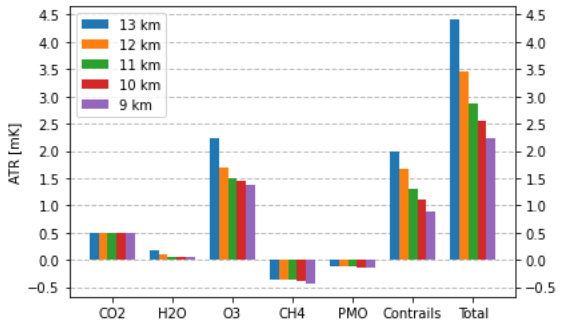

Figure 4.16: Altitude effects A350-900

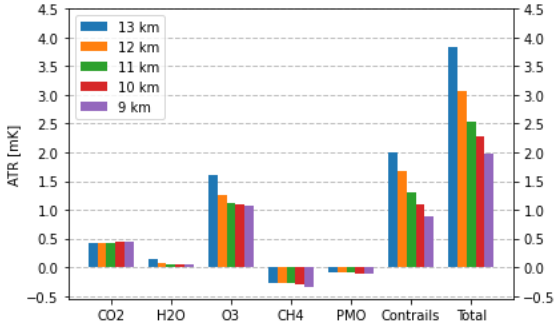

Figure 4.17: Altitude effects Flying V-900

Table 4.4: A350: Effects of varying altitude

Altitude [m]	Fuel consumption [g/pax-km]	EI NO_x [g/kg]	ATR [mK]
13000	20.26	19.69	4.41
12000	19.74	17.25	3.47
11000	19.70	15.59	2.86
10000	19.75	15.57	2.56
9000	20.04	15.80	2.23

Table 4.5: Flying V: Effects of varying altitude

Altitude [m]	Fuel consumption [g/pax-km]	EI NO_x [g/kg]	ATR [mK]
13000	17.36	16.54	3.83
12000	17.17	14.76	3.07
11000	17.37	13.55	2.54
10000	17.63	13.71	2.28
9000	18.05	14.06	1.98

The results presented in table 4.4 and table 4.5 show a significant upward trend in climate impact with increasing altitude for both aircraft. CO_2 is the exception and only changes slightly due to an increase of fuel flow when either aircraft deviates from it's design altitude. H_2O, NO_x and Contrails all show a substantial increase of climate impact at higher altitudes.

4.2.3. LOCAL EFFECTS

For studying the climate impact on specific locations in terms of latitude, four different climate zones are defined:

- Tropics, between equator and the tropics of Cancer/Capricorn
- Subtropics, between tropic of Cancer/Capricorn and 35 ° latitude
- Temperate zone, between 35 ° and (Ant)Arctic circle
- Frigid zone, between (Ant)Arctic circle and North/South-pole

The zones are also shown in fig. 4.18.

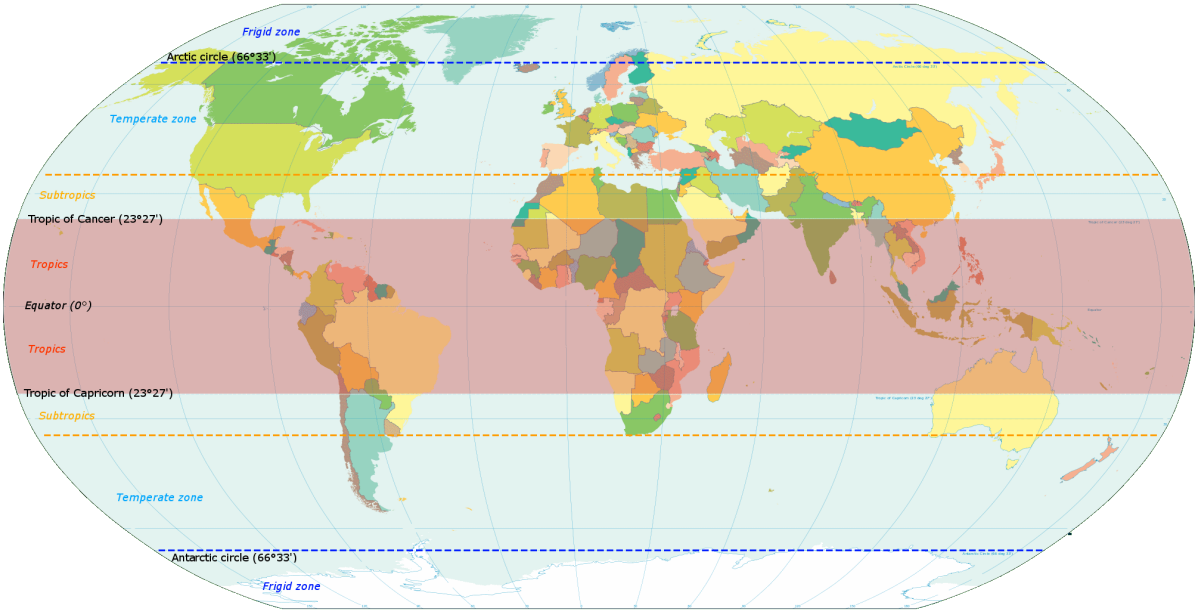

Figure 4.18: Climate zones

In fig. 4.19, fig. 4.20, fig. 4.21 and fig. 4.22, a number of differences in behaviour of the various climate agents are presented. For CO_2, no real differences are distinguished between the four zones. For H_2O however, the relative climate impact increases when going from the tropics to the poles. Impact from NO_x is higher near the equator than at the poles. Contrails show the opposite effect; they become more influential in terms of climate impact zones closer to the north and south pole.

Table 4.6: A350-900: climate impact per zone

Zone	Relative Distance	ATR [mK]	Relative ATR	ATR-distance ratio
Tropics	25%	0.39	17%	0.67
Subtropics	17%	0.31	14%	0.80
Temperate	54%	1.46	64%	1.18
Frigid	4%	0.13	6%	1.57
Global	100%	2.29	100%	1.00

Section 4.2.3 and section 4.2.3 emphasize the differences in behaviour of the climate agents at different climate zones. It is observed that the climate impact per flown kilometer increases when moving away from the equator. For the tropics and subtropics, the fraction of climate impact is smaller than the fraction of the total flown kilometers. For the temperate and frigid zones, the opposite holds; the fraction of climate impact is larger than the fraction of flown kilometers.

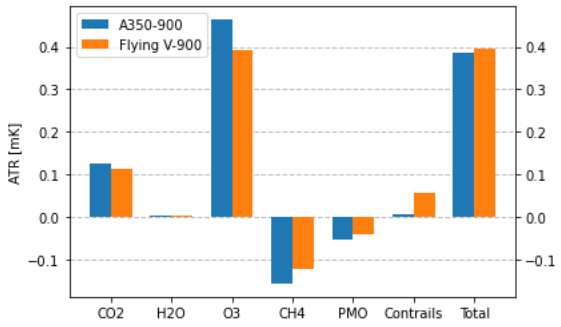

Figure 4.19: Climate impact at tropics

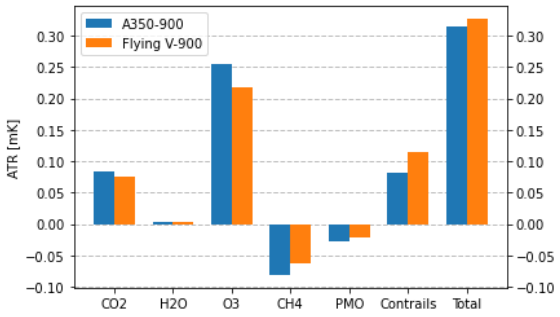

Figure 4.20: Climate impact at subtropics

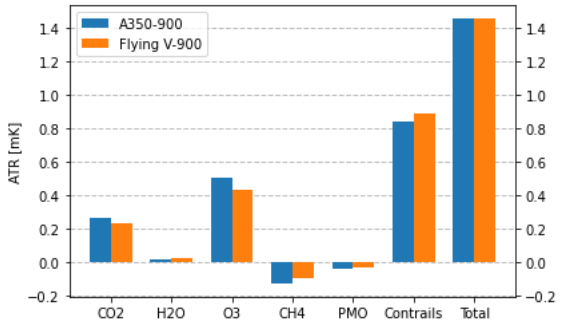

Figure 4.21: Climate impact at temperate zone

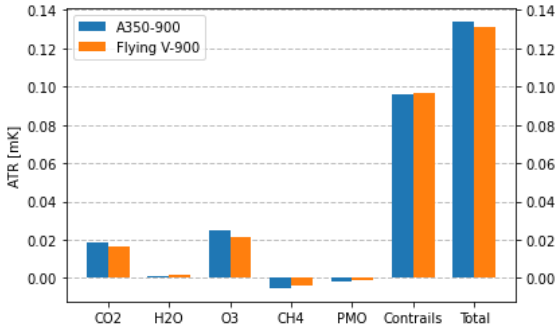

Figure 4.22: Climate impact at frigid zone

Table 4.7: Flying V-900: climate impact per zone

Zone	Relative Distance	ATR [mK]	Relative ATR	ATR-distance ratio
Tropics	25%	0.40	17%	0.69
Subtropics	17%	0.33	14%	0.83
Temperate	54%	1.46	63%	1.18
Frigid	4%	0.13	6%	1.54
Global	100%	2.31	100%	1.00

4.2.4. VARYING CH_4, CO_2 BACKGROUNDS

A nuance that must be mentioned for all results is that an assumption is made for the background concentrations of both methane and carbon dioxide in the decades ahead. How the concentration of these two greenhouse gasses develops is highly uncertain, so it is interesting to see what happens to the results when using different background scenarios. For CH_4, 13 alternative scenarios are available in AirClim, while for CO_2, 14 are available. Most of them follow a story line with particular features of economic growth and global population.

The default scenario is A1B, which is the fossil fuel balanced variant of the A1 family of story lines. The A1 story line describes a future world of rapid economic growth. Global population is assumed to peak halfway the century and declines afterwards. In terms of engineering, new and more efficient technology develops rapidly. The A2 story line assumes a heterogeneous world with a continuously increasing population. Technological and economic development is slower than in other scenarios. The B1 scenario is similar to the A1 scenario, but assumes changes in economic structures towards a service and information economy. This imposes a reduction in material intensity and promotion of resource-efficient technologies on a global scale. The B2 scenario emphasizes on local solutions to sustainability. It assumes continuous growth in global population, but not as rapidly as A2. [16]

The aforementioned scenarios all have an alternative as well, called preliminary marker. These scenarios were constructed due to uncertainties in the assumptions of the four storylines. These scenarios can help in mapping the uncertainty ranges of the results. The IS92a, IS92a/SAR and S&S scenarios are used in previous climate impact reports from the IPCC.

Following is the complete list of alternative scenarios. For CO_2, the S&S is an additional scenario. The

other ones are based on the same story line as the CH_4- background scenarios.

1. A1B: A1 variant balanced between fossil and non-fossil
2. A1T: non-fossil A1 variant
3. A1FI: fossil intensive A1 variant
4. A2
5. B1
6. B2
7. A1p: preliminary marker scenario
8. A2p: preliminary marker scenario
9. B1p: preliminary marker scenario
10. B2p: preliminary marker scenario
11. IS92a
12. IS92a/SAR
13. S&S
14. Constant

The A350-900 and the Flying V-900 were once again analyzed at design conditions, but now the end results with each background scenario are compared. The results with varying CO_2 backgrounds are shown in fig. 4.23 and fig. 4.24. The mean values have been plotted, while the results for each scenario are scattered.

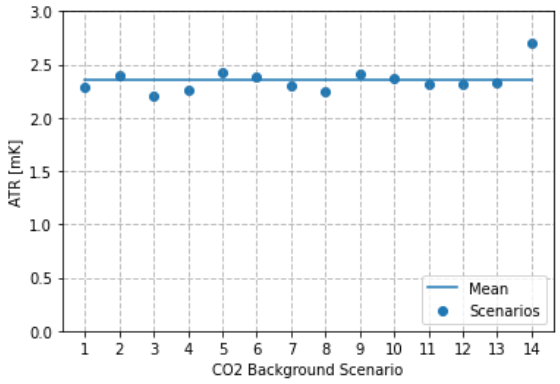

Figure 4.23: A350: Climate impact at multiple CO_2 background scenarios

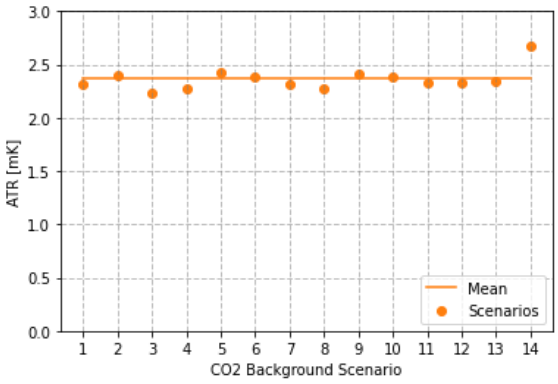

Figure 4.24: Flying V: Climate impact at multiple CO_2 background scenarios

The differences in total climate impact can be analyzed. The biggest outlier in this figure is the constant variant (14), which shows a difference with respect to the means of 16% and 13% for the A350 and the Flying V, respectively. This scenario is the only one that predicts a higher climate impact from the A350 than the Flying V and this is most probably due to a larger relative influence of CO_2, which is emitted more by the A350 than the Flying V. Though this deviation is quite large, it must be stated that the constant background CO_2 scenario is not a realistic scenario. The other scenarios remain within 6% of the mean. The differences in climate impact between the two aircraft are between 0% and 1.2%.

The results for varying CH_4-backgrounds are shown similarly in fig. 4.25 and fig. 4.26. The mean values have been plotted, while the results for each scenario are scattered. The different methane scenarios did not result in major outliers, with all of the scenarios staying within 4% of the mean. The differences in climate impact between the A350 and the Flying V are less than 2% for all scenarios, with the A350 outperforming the Flying V in all scenarios.

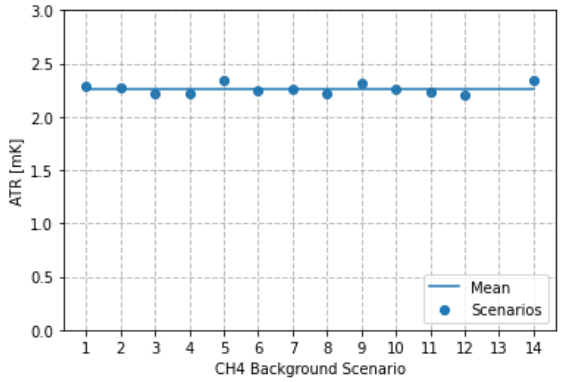

Figure 4.25: A350: Climate impact at multiple CH4 background scenarios

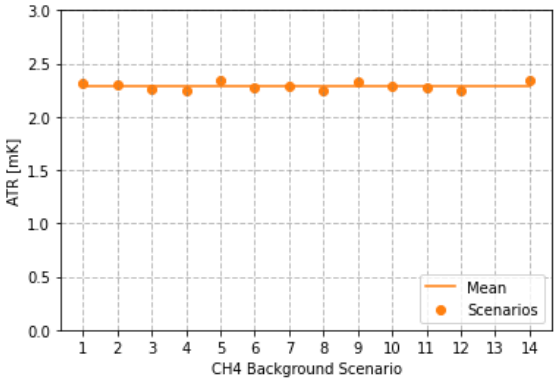

Figure 4.26: Flying V: Climate impact at multiple CH4 background scenarios

4.2.5. VARYING FUEL SCENARIOS

Similar to the different background scenarios for CO_2 and CH_4, it is also possible to see what happens to the results when varying the fuel scenario. The different available scenarios are listed:

1. Fa1
2. C20_50
3. C2000
4. N2015
5. Eab
6. Eah
7. N1999
8. N2000
9. C20_30
10. Exp1
11. Exp2
12. Exp3
13. Exp4

Each scenario represents a different global fuel emission development scheme. How these scenarios develop over time is represented in fig. 4.27, fig. 4.28, fig. 4.29, fig. 4.30 and fig. 4.31.

The climate assessment module has been run once again, by inputting the emission inventories of the design conditions, but now selecting the different fuel scenarios in AirClim. Scenario's 2, 4, 7, 8, and however returned NaN values for temperature change by 2150. This is most probably due to fuel scenarios going to zero after certain points in the future, yielding singularities in the simulations.

The results of the different fuel scenarios are plotted in fig. 4.32 and fig. 4.33. It is observed that the variance in results is small, with the default scenario Fa1 being the biggest outlier with 11$ for both aircraft. When comparing the climate impact of both aircraft to each other for all scenarios, the results show minimal variation. The differences are all within 1.2% and in favour of the A350.

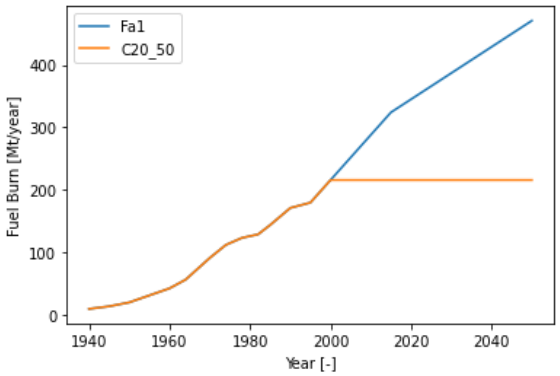

Figure 4.27: Fuel scenarios 1 and 2

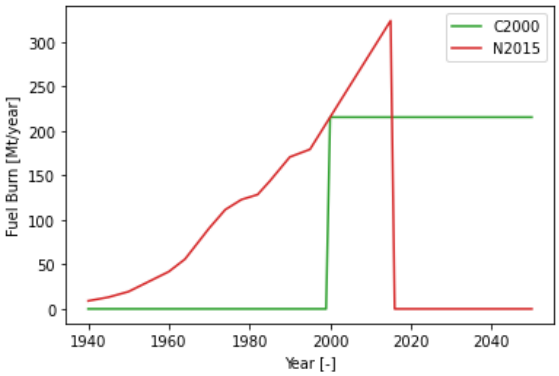

Figure 4.28: Fuel scenarios 3 and 4

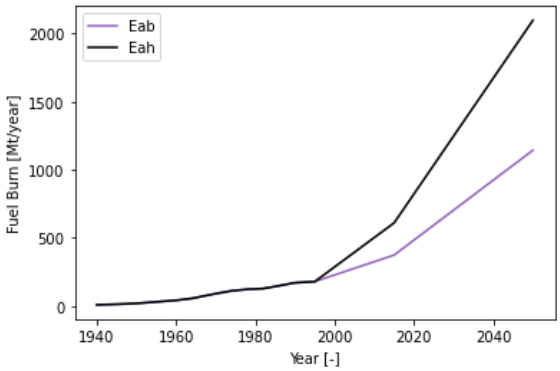

Figure 4.29: Fuel scenarios 5 and 6

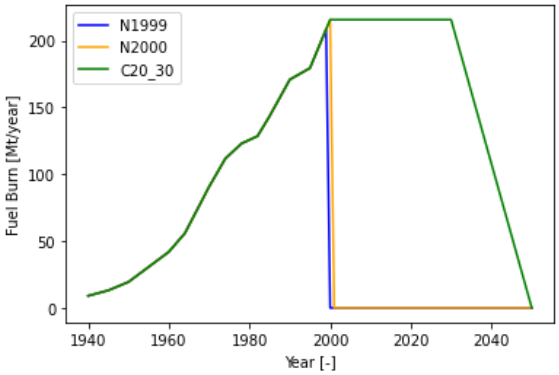

Figure 4.30: Fuel scenarios 7, 8 and 9

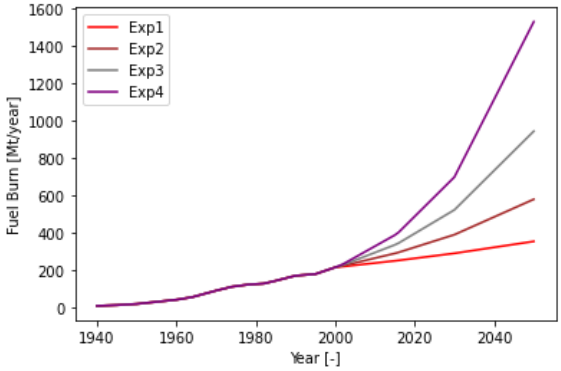

Figure 4.31: Fuel scenarios 10, 11, 12 and 13

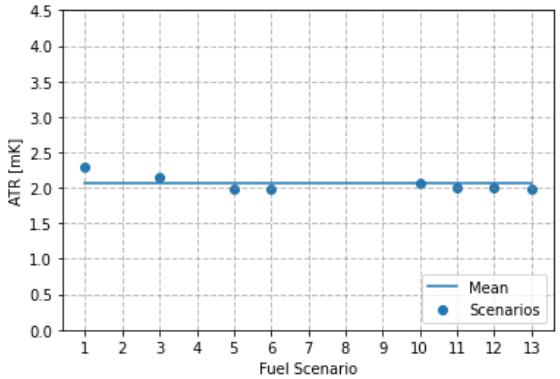

Figure 4.32: A350: Climate impact at multiple fuel scenarios

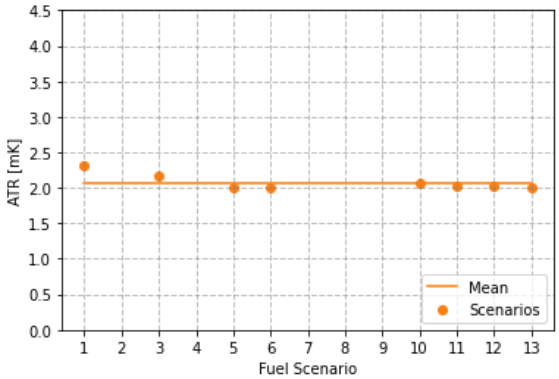

Figure 4.33: Flying V: Climate impact at multiple fuel scenarios

4.3. UNCERTAINTIES

The results discussed in this section are from the Monte Carlo simulations as discussed in section 3.4.2. Once again, the design conditions case is considered. The "best estimates" are the same results elaborated in section 4.1.3. The MC simulations predict the uncertainties of the results with 10000 random samples deviating from the best estimates.

The probability distributions with a 90% confidence interval of the total ATR are documented in the histograms of fig. 4.34 and fig. 4.35. The lower and upper limits for the A350-900 confidence interval are 1.66 mK and 2.93 mK, respectively. For the Flying V-900, these are 1.66 mK and 2.96 mK. Histograms of the individual climate agents are listed in appendix D.

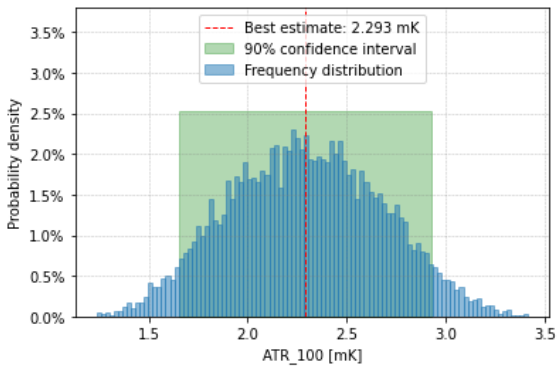

Figure 4.34: A350: Histogram total ATR

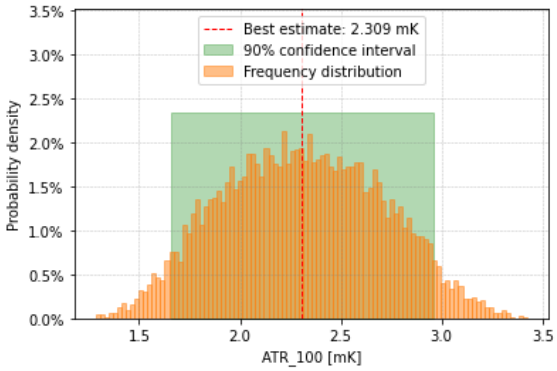

Figure 4.35: Flying V: Histogram total ATR

The temperature change development over time is once again shown in fig. 4.36 and fig. 4.37, though now with the uncertainty ranges added to it.

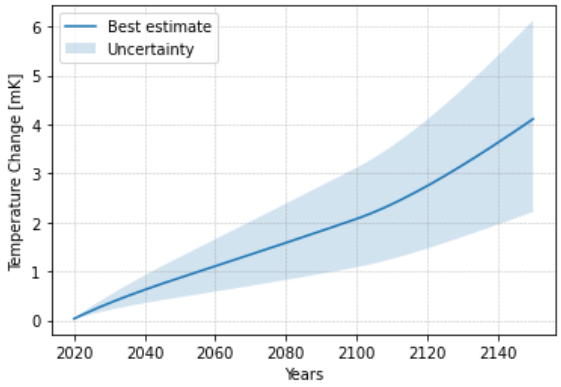

Figure 4.36: A350: Temperature change development

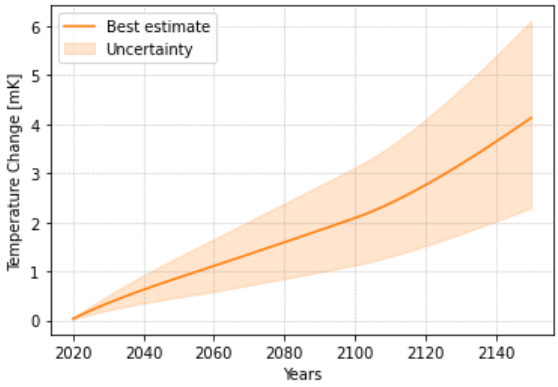

Figure 4.37: Flying V: Temperature change development

When zooming in on the uncertainty ranges of the different climate effects, it is useful to consider the box plots in fig. 4.38 and fig. 4.39.

Table 4.8: A350: Uncertainties per climate agent

Climate Agent	Best estimate ATR [mK]	Lower limit ATR [mK]	Upper limit ATR [mK]
CO_2	0.49	0.44	0.54
H_2O	0.02	0.02	0.03
O_3	1.25	0.87	1.62
CH_4	-0.37	-0.61	-0.17
PMO	-0.12	-0.24	-0.04
Contrails	1.03	0.47	1.68
Total	2.29	1.24	3.42

Table 4.9: Flying V: Uncertainties per climate agent

Climate Agent	Best estimate ATR [mK]	Lower limit ATR [mK]	Upper limit ATR [mK]
CO_2	0.44	0.40	0.49
H_2O	0.03	0.02	0.04
O_3	1.07	0.75	1.39
CH_4	-0.29	-0.48	-0.13
PMO	-0.10	-0.19	-0.03
Contrails	1.16	0.53	1.90
Total	2.31	1.28	3.43

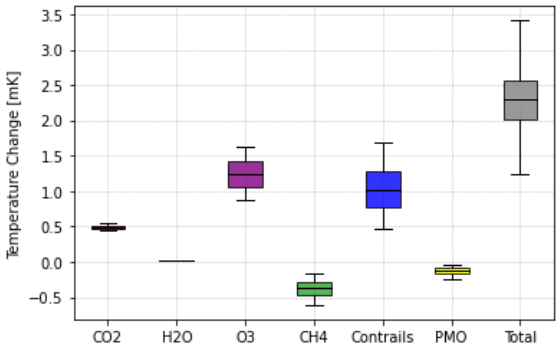

Figure 4.38: A350: Box plot uncertainties climate agents

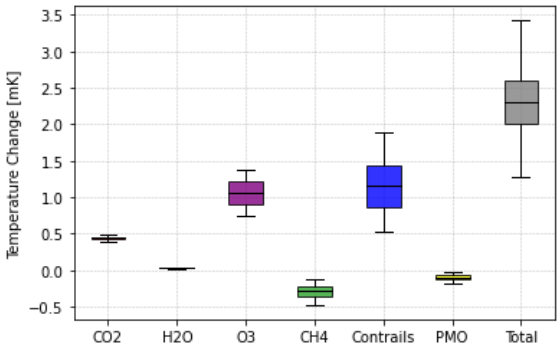

Figure 4.39: Flying V: Box plot uncertainties climate agents

4.4. OPTIMIZATION STUDY

Previous results, especially in those in section 4.2.2, have shown a correlation between altitude and climate impact. The higher an aircraft operates, the more temperature change is triggered due to increased radiative forcing. NO_x, water vapour and contrails are the three main contributors to this effect.

The Flying V's design intent is to develop an aircraft which is superior to the A350 in terms of climate impact. However, in design conditions this is not the case. Therefore, an optimization study has been performed to see if an optimum altitude can be determined for minimum climate impact, while keeping the fuel consumption at an acceptable level.

For both aircraft, the temperature change and fuel consumption have been determined for altitudes from 13000 down to 6000 meters, to see how much benefit can be achieved by the effects of lowering altitude. The plot is shown in fig. 4.40.

It becomes clear in this figure that climate impact keeps decreasing when lowering altitude. Fuel consumption increases, but at a much lower rate than the decrease in ATR. The slope of the ATR for both aircraft show a steep increase above at about 11500 meters altitude. This is most likely due to the tropopause, below which the effects from NO_x emissions decrease.

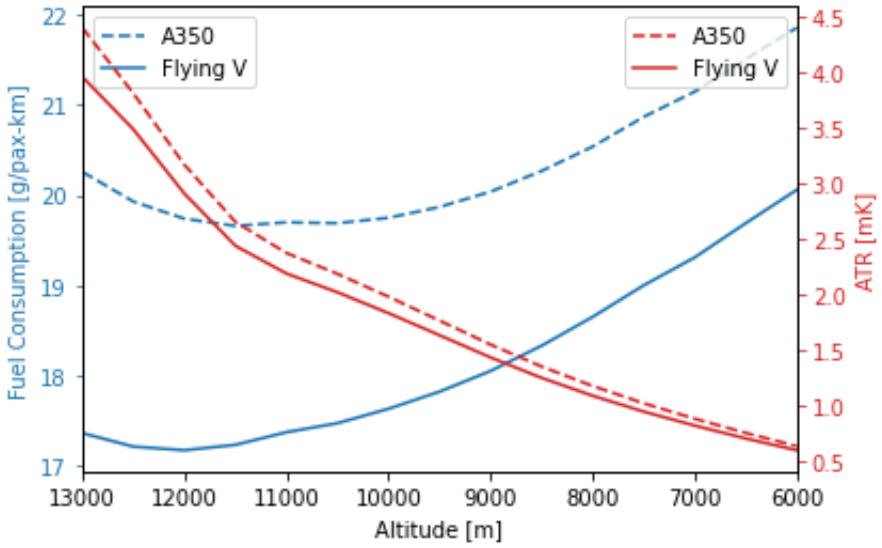

Figure 4.40: Fuel consumption and temperature change vs. altitude

5

Conclusions & Recommendations

The final chapter of this thesis report will elaborate on the conclusions and recommendations that follow from the results of this research. In section 5.1, the research questions will be answered. Section 5.2 will make recommendations for future aircraft design or climate impact research.

5.1. Conclusions

The research question to be answered in this thesis is:
How does the Flying V aircraft perform in terms of climate impact and mitigation capabilities compared to a conventional tube-and-wing aircraft?
The literature study phase of this project reviewed the climate effects related to the two aircraft.

- CO_2 emission
- NO_x emission, causing O_3-production, CH_4 lifetime reduction and Primary Mode Ozone
- H_2O emission
- Contrails (Aerodynamic and Exhaust). In this research, only exhaust contrails have been considered.
- Aerosols (sulphate and soot). Though these particles have a direct climate effect, only the indirect effects in contrail climate impact have been considered in this research.

The average temperature response for the A350-900 and Flying V are 2.29 mK and 2.31 mK, respectively. This yields a difference in design conditions of just 1%. Flying V-900 outperforms the A350-900 in terms of fuel consumption, a lower amount of CO_2 and NO_x emission. However, the higher altitude of the Flying V-900 imposes a larger impact mainly from contrails, leading to a higher temperature change response.

The altitude analysis showed a clear trend downwards in terms of climate impact when the operating altitude is lowered. This applies to both aircraft. The optimization study analyzes altitudes even further down to 6 km altitude, where the ATR is reduced by 72% compared to the design conditions for the A350 and 74% for the Flying V.

Though lowering altitude decreases the climate impact, it also increases the fuel consumption. So the fuel performance of both aircraft decreases when deviating from the design conditions. The change in fuel consumption is however smaller than the change in climate impact. So although it may seem counter-intuitive, from a climate impact perspective, it is better for both aircraft to compromise fuel consumption for the sake of reducing the radiative forcing and thus temperature change due to the emissions. This conclusion applies to both aircraft.

The research question can once again be considered. The answer is quite simple. The Flying V and the baseline A350 aircraft perform almost similar in terms of climate impact. In terms of mitigation capabilities, the Flying V performs better. The Flying V burns less fuel than the A350 on the entire altitude and Mach number spectrum, imposing less emissions and thus less climate impact if both aircraft are operating at identical conditions.

5.2. RECOMMENDATIONS

A much repeated feature in this research is that operating at higher altitudes comes at a price. Although fuel consumption is generally better at higher altitudes, often it is still favorable to fly at lower altitudes to reduce climate impact. This counts for both the A350 aircraft as the Flying V.

The conclusions section mentioned that the Flying V and the A350 perform comparable in terms of climate impact, so it is advised to pursue the design of the Flying V at an adjusted altitude. The Flying V or any novel aircraft concept for that matter could benefit from designing for lower altitudes. The optimization study concluded that climate impact could reduce by a factor 4 when choosing to fly at 6000 meters instead of the current flight corridor for medium to long range flights.

It is recognized that an average temperature response reduction can be achieved when flying off-design at lower altitudes. This comes however at an economic penalty of higher fuel consumption, which may encounter resistance from an economic perspective. Going forward it is recommended to map minimization of ATR versus operating cost of the aircraft.

It must also be noted however that the main focus of this research has been to perform a case study between two aircraft. With that focus in mind, the relative difference between the two has been considered more important than the absolute values of the results in terms of climate impact and fuel consumption. Both aircraft have been researched using the same methodology.

For future research regarding the Flying V, it is recommended to improve the accuracy of the drag polar prediction. In this research, the zero-lift drag and lift-dependent drag coefficients have been computed using empirical relations. The accuracy of the drag polars for both aircraft could be improved by doing thorough analysis in for example an Athena Vortex Lattice analysis.

For further research about designing and operating aircraft at lower cruise altitudes, it is advised to investigate the validity of this hypotheses with different climate assessment modules. In this research, AirClim has been used, which relies on heavy assumptions such as the neglecting meteorological variance and exact time of emission during the day. It is recommended to evaluate the effects of these assumptions to verify the effectiveness of this study.

BIBLIOGRAPHY

[1] Grewe, V. and Stenke, A., *Airclim: an efficient tool for climate evaluation of aircraft technology,* Atmospheric Chemistry and Physics **8**, 4621 (2011).

[2] Lee, D.S. et al, *The contribution of global aviation to anthropogenic climate forcing for 2000 to 2018,* Atmospheric Environment **244** (2021).

[3] Gangoli Rao, A., Yin, F. and Werij, H., *Energy transition in aviation: the role of cryogenic fuels,* Aerospace — Open Access Aeronautics and Astronautics Journal **7 (12)**, 1 (2020).

[4] Wilcox, L.J. et al, *Radiative forcing due to aviation water vapour emissions,* Atmospheric Environment **8** (2012).

[5] Köhler, M.O. et al, *Impact of perturbations to nitrogen oxide emissions from global aviation,* Journal of the Geophysical Research **113** (2008).

[6] Rädel, G. et al, *Radiative forcing by persistent contrails and its dependence on cruise altitudes,* Journal of the Geophysical Research **113** (2007).

[7] Benad, J., *The Flying V: An entirely new aircraft configuration,* in *Deutscher Luft- und Raumfahrtkongress 2015* (2015).

[8] E. Obert, *Aerodynamic Design of Transport Aircraft*, First ed. (Delft University Press, Delft, the Netherlands, 2009).

[9] Faggiano, F., *Aerodynamic Design Optimization of a Flying V Aircraft*, Master's thesis, Delft University of Technology, Delft (2016).

[10] Lee, D.S., *The current state of scientific understanding of the non-CO2 effects of aviation on climate*, Tech. Rep. (Department for Transport, 2018).

[11] Reekers, M.J.D., *Literature Study Report: Climate effects of Flying V aircraft,* (2020), Delft University of Technology.

[12] Solomon, S. et al, *Climate Change 2007: The Physical Science Basis. Contribution of Working Group I to the Fourth Assessment Report of the Intergovernmental Panel on Climate Change*, Tech. Rep. (IPCC, Cambridge, United Kingdom and New York, NY, USA, 996 pp., 2007).

[13] *ICAO Long-Term Traffic Forecasts Passenger and Cargo*, International Civil Aviation Organization, Montreal, Quebec, Canada (2016).

[14] Grewe, V. and Dedoussi, I., *AE4462-17 Aircraft emissions and Climate Effects Lecture Notes,* Delft University of Technology (2019).

[15] Lee, D.S. et al, *Transport impacts on atmosphere and climate: Aviation,* Atmospheric Environment **44**, 4678 (2010).

[16] Davidson, O. et al, *IPCC Special report Emissions Scenarios*, Tech. Rep. (IPCC, Cambridge, United Kingdom and New York, NY, USA, 1535 pp., 2000).

[17] Bowman, C.T., *Control of combustion-generated nitrogen oxide emissions: technology driven by regulation,* in *Symposium (International) on Combustion* (Pittsburgh, PA, USA, 1992) pp. 859–878.

[18] Jones, I.T.N., *Photolysis of nitrogen dioxide:,* J. Chem. Phys **59** (1973).

[19] Gierens, K., *Physical fundamentals of contrail formation - the Schmidt-Appleman criterion and the role of particles*, Tech. Rep. (Institut für Physik der Atmosphäre, DLR Oberpfaffenhofen, 2014).

[20] Jensen, E.J. et al, *Environmentall conditions required for contrail formation and persistence,* Journal of geophysiical research **103**, 3929 (1998).

[21] Schumann, U., *On conditions for contrail formation from aircraft exhausts,* Meteorol. Z. **5**, 4 (1996).

[22] Kärcher, B. et al, *Aerodynamic contrails: Microphysics and optical properties,* Journal of the Atmospheric Sciences **66**, 227 (2009).

[23] Brown, R.C. and Anderson, M.R., *Aircraft exhaust sulfur emissions,* Geophys. Res. Lett. **23**, 3603–3606 (1996).

[24] Bond, T.C. et al, *Bounding the role of black carbon in the climate system: A scientific assessment,* J. Geophys. Res. **118**, 5380 (2013).

[25] Schwartz, E. and Kroo, I.M., *Aircraft design: Trading cost and climate impact,* in *47th AIAA Aerospace Sciences Meeting* (Orlando, FL, USA, 2009).

[26] Bahr, D.W. et al, *Aircraft turbine engine nox emission abatement,* in *Unsteady Combustion* (Springer, Dordrecht, the Netherlands, 1996) pp. 243–264.

[27] Huszar, P. et al, *Modeling the climate impact of aviation,* Atmospheric Chemistry and Physics **13**, 10027 (2013).

[28] Unger, N. et al, *Mid-21st century chemical forcing of climate by the civil aviation sector,* Geophysical Research Letters **40**, 641 (2013).

[29] Stocker, T.F. et al, *Climate Change 2013: The Physical Science Basis. Contribution of Working Group I to the Fifth Assessment Report of the Intergovernmental Panel on Climate Change*, Tech. Rep. (IPCC, Cambridge, United Kingdom and New York, NY, USA, 1535 pp., 2013).

[30] Freeman, S. et al, *Trading off aircraft fuel burn and nox emissions for optimal climate policy,* Environmental Science and Technology **52**, 2498 (2018).

[31] Fuglesvedt, J.S. et al, *Transport impacts on atmosphere and climate: Metrics.* Atmospheric Environment **44**, 4648 (2010).

[32] Allen, M. et al, *A solution to the misrepresentations of co2-equivalent emissions of short-lived climate pollutants under ambitious mitigation,* npj Climate and Atmospheric Science **1** (2018).

[33] Nuic, A. et al, *Bada: An advanced aircraft performance model for present and future atm systems,* International Journal of Adaptive Control and Signal Processing (2020).

[34] Junzi, S, *Open Aircraft Performance Modeling: Based on an Analysis of Aircraft Surveillance Data*, Ph.D. thesis, Delft University of Technology (2019).

[35] Torenbeek, E., *Blended wing body and all-wing airliners,* in *European Workshop on Aircraft Design Education (EWADE)* (Samara, Russia, 2007).

[36] Cappuyns, T., *Handling Qualities of a Flying V Configuration*, Master's thesis, Delft University of Technology, Delft (2019).

[37] Bourget, G., *The effect of landing gear implementation on Flying V aerodynamics, stability and controllability*, Master's thesis, Delft University of Technology, Delft (2020).

[38] Empelen, S. van, *Engine Integration of the Flying V: Quantification of Engine Integration Effects using Wind Tunnel Experiments*, Master's thesis, Delft University of Technology, Delft (2020).

[39] Hillen, M., *Parametrisation of the Flying V Outer Mold Line*, Master's thesis, Delft University of Technology, Delft (2020).

[40] Oosterom, W., *Flying V family design*, Master's thesis, Delft University of Technology, Delft (2021).

[41] E. Torenbeek, *Advanced Aircraft Design: Conceptual Design, Analysis, and Optimization of Subsonic Civil Airplanes*, 2nd ed. (Wiley, Hoboken, NJ, USA, 2013).

[42] *AIRCRAFT CHARACTERISTICS AIRPORT AND MAINTENANCE PLANNING: A350*, Airbus Corporation (2016).

[43] European Union Aviation Safety Agency, *ICAO Aircraft Engine Emissions Databank,* Issue 28B implemented on website (2021).

[44] *Fuel Flow Method 2 for Estimating Aircraft Emissions*, SAE Technical Paper No. 2006-01-1987 (Boeing Corporation, 2006).

[45] Hein, R. et al, *Results of an interactively coupled atmospheric chemistry-general circulation model: Comparison with observations,* Annual Geophysics **19**, 435 (2001).

A

APPENDIX A: WETTED AREA A350-900

Symbol	Description	Dimension	Unit
h_{fus}	Fuselage height	6.09	m
w_{fus}	Fuselage width	5.96	m
l_{fus}	Fuselage length	65.26	m
t/c_{wing}	Thickness-to-chord ratio wing	0.115	-
k_Q	Volume factor	0.95	-
b	Wingspan	64.75	m
c_{root}	Root chord	13.47	m
c_{kink}	Kink chord	8.12	m
c_{tip}	Tip chord	1.72	m
$b/2_{inboard}$	Semispan inboard	7.52	m
$b/2_{ouboard}$	Semispan outboard	21.86	m
t/c_{VT}	Thickness-to-chord ratio vertical tail	0.092	-
$c_{tip,VT}$	Tip chord vertical tail	3.04	m
$c_{root,VT}$	Root chord vertical tail	7.79	m
b_{VT}	Span vertical tail	9.42	m
t/c_{HT}	Thickness-to-chord ratio horizontal tail	0.103	-
$c_{tip,HT}$	Tip chord horizontal tail	2.46	m
$c_{root,HT}$	Root chord horizontal tail	6.21	m
b_{HT}	Span horizontal tail	19.29	m
l_n	Nacelle length	6.4	m
D_n	Nacelle diameter	3.52	m
l_l	Front nacelle length	1.4	m
D_{hl}	Fan cowling front inner diameter	3.17	m
D_{ef}	Fan cowling aft diameter	2.82	m
l_g	Gas generator length	0.56	m
D_g	Gas generator cowling front diameter	1.68	m
D_{eg}	Gas generator cowling aft diameter	1.68	m
l_p	Plug length	1.53	m
D_p	Plug diameter	1.35	m

Table A.1: Geometric dimensions A350-900

For calculating the wetted area of the fuselage, first the fuselage diameter d_{fus} is computed:

$$d_{fus} = \sqrt{h_{fus} \cdot w_{fus}} \tag{A.1}$$

Then, the wetted area of the front of the fuselage $S_{fus,front}$ can be estimated:

$$S_{fus,front} = \frac{\pi}{4} * w_{fus} * h_{fus} \tag{A.2}$$

The volume of the fuselage Q_{fus} is estimated with:

$$Q_{fus} = S_{fus,front} * (l_{fus} - 2 * d_{fus}) \tag{A.3}$$

The resulting fuselage wetted area $S_{wet,fus}$ is then:

$$S_{wet,fus} = 2\left(2\pi \frac{l_{fus}}{d_{fus}}\right)^{\frac{1}{3}} Q_{fus}^{\frac{2}{3}} \left(1 + \frac{1}{(\frac{l_{fus}}{d_{fus}})^2}\right) \tag{A.4}$$

For both the inboard and the outboard wing, the following relations are used. First the taper ratio λ is obtained.

$$\lambda_{inboard} = \frac{c_{kink}}{c_{root}} \tag{A.5}$$

$$\lambda_{outboard} = \frac{c_{tip}}{c_{kink}} \tag{A.6}$$

The reference area S_{ref} is:

$$S_{ref,inboard} = 2(b/2)_{inboard} \frac{c_{root} + c_{kink}}{2} \tag{A.7}$$

$$S_{ref,outboard} = 2(b/2)_{outboard} \frac{c_{kink} + c_{tip}}{2} \tag{A.8}$$

The wing volume Q_W is then computed along with the aspect ratio A_W:

$$A_W = \frac{b^2}{S_{ref}} \tag{A.9}$$

$$Q_W = (k_Q \frac{t/c_{wing}}{\sqrt{1+\lambda}}) S_{ref} \sqrt{\frac{S_{ref}}{A_W}} \tag{A.10}$$

The wetted area of the wing surfaces $S_{wet,wing}$ is computed by:

$$S_{wet,wing} = (2 + 0.5 t/c_{wing}) \left(\frac{Q_W * \sqrt{A_W * (1+\lambda)}}{k_Q * t/c_{wing}}\right)^{\frac{2}{3}} \tag{A.11}$$

The vertical and horizontal tail surfaces are also considered as wing surfaces, so the same relations (A.5 - A.11) are used to compute the wetted areas for these components.
The wetted areas for the nacelles (or cowlings) are computed as follows. First, the fan cowling, $S_{wet,fan-cowling}$ is considered.

$$S_{wet,fan-cowling} = l_n D_n \left(2 + 0.35 \frac{l_l}{l_n} + 0.8 \frac{l_l D_{hl}}{l_n D_n} + 1.15\left(1 - \frac{l_l}{l_n}\right) \frac{D_{ef}}{D_n}\right) \tag{A.12}$$

The wetted area for the gas generator cowling $S_{wet,gasgen-cowling}$ is:

$$S_{wet,gasgen-cowling} = \pi l_g D_g \left(1 - \frac{1}{3} \cdot (1 - \frac{D_{eg}}{D_g}) \cdot \left(1 - 0.18\left(\frac{D_g}{l_g}\right)^{\frac{5}{3}}\right)\right) \tag{A.13}$$

For the pylons, the following relation is used:

$$S_{wet-pylon} = S_{wet-cowling} \cdot 0.2 \tag{A.14}$$

The total wetted area is computed by adding the wetted areas of all components together:

$$S_{wet} = S_{wet,wing} + S_{wet,fus} + S_{wet,VT} + S_{wet,HT} + S_{wet,cowling} + S_{wet,pylon} \tag{A.15}$$

B

APPENDIX B: A350 CITY-PAIRS

Table B.1: A350 City-pairs (1/5)

Airline	Origin	Destination	Destination 2	Type
Aeroflot	Moscow Sheremetyevo	Osaka Kansai		900
Aeroflot	Moscow Sheremetyevo	London Heathrow		900
Air Caraibes	Paris Orly	Cayenne		900
Air Caraibes	Paris Orly	Fort-de-France		1000
Air Caraibes	Paris Orly	Pointe-a-Pitre		1000
Air China	Beijing Capital	Chengdu		900
Air China	Beijing Capital	Guangzhou		900
Air China	Beijing Capital	Shanghai Hongqiao		900
Air China	Shanghai Pudong	Osaka Kansai		900
Air China	Beijing Capital	Frankfurt		900
Air France	Paris Charles de Gaulle	Bamako	Abidjan	900
Air France	Paris Charles de Gaulle	Bamako	Lagos	900
Air France	Paris Charles de Gaulle	Cairo		900
Air France	Paris Charles de Gaulle	Dubai		900
Air France	Paris Charles de Gaulle	Ho Chi Minh City		900
Air France	Paris Charles de Gaulle	Mumbai		900
Air France	Paris Charles de Gaulle	Atlanta		900
Air France	Paris Charles de Gaulle	Toronto		900
Air France	Paris Charles de Gaulle	Sao Paulo Guarulhos		900
Air Mauritius	Mauritius	Antananarivo		900
Air Mauritius	Mauritius	Delhi		900
Air Mauritius	Mauritius	Mumbai		900
Air Mauritius	Mauritius	London Heathrow		900
Air Mauritius	Mauritius	Paris Charles de Gaulle		900
Asiana	Seoul Incheon	Sydney		900
Asiana	Seoul Incheon	Frankfurt		900
Asiana	Seoul Incheon	London Heathrow		900
Asiana	Seoul Incheon	Los Angeles		900
Asiana	Seoul Incheon	New York JFK		900
Asiana	Seoul Incheon	San Francisco		900
Asiana	Seoul Incheon	Seattle Tacoma		900
British Airways	London Heathrow	Bangalore		1000
British Airways	London Heathrow	Dubai		1000
British Airways	London Heathrow	Tel Aviv		1000
British Airways	London Heathrow	Boston		1000
British Airways	London Heathrow	Philadelphia		1000

Table B.2: A350 City-pairs (2/5)

Airline	Origin	Destination	Destination 2	Type
British Airways	London Heathrow	Washington Dulles		1000
Cathay Pacific	Hong Kong	Ho Chi Minh City		900
Cathay Pacific	Hong Kong	Taipei Taoyuan		1000
Cathay Pacific	Hong Kong	Tel Aviv		1000
Cathay Pacific	Hong Kong	Melbourne		900
Cathay Pacific	Hong Kong	Perth		1000
Cathay Pacific	Hong Kong	Sydney		900
Cathay Pacific	Hong Kong	Amsterdam Schiphol		1000
Cathay Pacific	Hong Kong	Frankfurt		1000
Cathay Pacific	Hong Kong	London Heathrow		1000
Cathay Pacific	Hong Kong	Manchester		1000
Cathay Pacific	Hong Kong	Los Angeles		1000
Cathay Pacific	Hong Kong	New York JFK		1000
Cathay Pacific	Hong Kong	San Francisco		900
Cathay Pacific	Hong Kong	Toronto		1000
China Airlines	Taipei Taoyuan	Bangkok Suvarnabhumi		900
China Airlines	Taipei Taoyuan	Hanoi		900
China Airlines	Taipei Taoyuan	Jakarta		900
China Airlines	Taipei Taoyuan	Brisbane		900
China Airlines	Taipei Taoyuan	Melbourne		900
China Airlines	Taipei Taoyuan	Amsterdam		900
China Airlines	Taipei Taoyuan	Frankfurt		900
China Airlines	Taipei Taoyuan	London Gatwick		900
China Airlines	Taipei Taoyuan	London Heathrow		900
China Airlines	Taipei Taoyuan	Vancouver		900
China Eastern	Shanghai Pudong	Xi'an	Madrid	900
China Eastern	Hangzhou	Sydney		900
China Eastern	Nanjing	Vancouver		900
China Southern	Guangzhou	Beijing Capital		900
China Southern	Guangzhou	Shanghai		900
China Southern	Guangzhou	Paris Charles de Gaulle		900
Delta Air Lines	Atlanta	Johannesburg	Cape Town	900
Delta Air Lines	Atlanta	Seoul Incheon		900
Delta Air Lines	Detroit	Seoul Incheon	Shanghai Pudong	900
Delta Air Lines	Detroit	Shanghai Pudong		900
Delta Air Lines	Los Angeles	Shanghai Pudong		900
Delta Air Lines	Atlanta	Tokyo Haneda		900
Delta Air Lines	Detroit	Tokyo Haneda		900
Delta Air Lines	Los Angeles	Tokyo Haneda		900
Delta Air Lines	Minneapolis St Paul	Tokyo Haneda		900
Delta Air Lines	Los Angeles	Sydney		900
Delta Air Lines	Detroit	Amsterdam		900
Delta Air Lines	Detroit	Paris Charles de Gaulle		900
Ethiopian Airlines	Addis Ababa	Abuja		900
Ethiopian Airlines	Addis Ababa	Cape Town		900
Ethiopian Airlines	Addis Ababa	Harare	Lusaka	900
Ethiopian Airlines	Addis Ababa	Kilimanjaro	Zanzibar	900
Ethiopian Airlines	Addis Ababa	Lusaka	Harare	900
Ethiopian Airlines	Addis Ababa	Chengdu		900
Ethiopian Airlines	Addis Ababa	Dubai		900
Ethiopian Airlines	Addis Ababa	Shanghai Pudong		900
Ethiopian Airlines	Addis Ababa	Frankfurt		900
Ethiopian Airlines	Addis Ababa	Paris CDG		900

Table B.3: A350 City-pairs (3/5)

Airline	Origin	Destination	Destination 2	Type
Fiji Airways	Nadi	Auckland		900
Fiji Airways	Nadi	Sydney		900
Fiji Airways	Nadi	Los Angeles International		900
Finnair	Helsinki	Hong Kong		900
Finnair	Helsinki	Krabi		900
Finnair	Helsinki	Nanjing		900
Finnair	Helsinki	Phuket		900
Finnair	Helsinki	Seoul Incheon		900
Finnair	Helsinki	Shanghai Pudong		900
Finnair	Helsinki	Tokyo Narita		900
Finnair	Helsinki	London Heathrow		900
French Bee	Paris Orly	St Denis de la Reunion		900
French Bee	Paris Orly	Newark		900
Hainan Airlines	Beijing Capital	Boston		900
Iberia	Madrid	Tokyo Narita		900
Iberia	Madrid	London Heathrow		900
Iberia	Madrid	Los Angeles		900
Iberia	Madrid	Bogota		900
Iberia	Madrid	Buenos Aires Ezeiza		900
Iberia	Madrid	Lima		900
Iberia	Madrid	Quito		900
Iberia	Madrid	Santiago de Chile		900
Japan Airlines	Tokyo Haneda	Fukuoka		900
Japan Airlines	Tokyo Haneda	Okinawa Naha		900
Japan Airlines	Tokyo Haneda	Sapporo New Chitose		900
LATAM Brasil	Sao Paulo Guarulhos	Johannesburg		900
LATAM Brasil	Sao Paulo Guarulhos	Frankfurt		900
LATAM Brasil	Sao Paulo Guarulhos	Madrid		900
LATAM Brasil	Sao Paulo Guarulhos	Paris Charles de Gaulle		900
Lufthansa	Munich	Cape Town		900
Lufthansa	Munich	Beijing Capital		900
Lufthansa	Munich	Delhi		900
Lufthansa	Munich	Mumbai		900
Lufthansa	Munich	Osaka Kansai		900
Lufthansa	Munich	Seoul Incheon		900
Lufthansa	Munich	Shanghai Pudong		900
Lufthansa	Frankfurt	Tokyo Haneda		900
Lufthansa	Munich	Tokyo Haneda		900
Lufthansa	Berlin Tegel	Munich		900
Lufthansa	Munich	Charlotte		900
Lufthansa	Frankfurt	Chicago O'Hare		900
Lufthansa	Munich	Chicago O'Hare		900
Lufthansa	Frankfurt	Los Angeles		900
Lufthansa	Munich	Los Angeles		900
Lufthansa	Munich	Miami		900
Lufthansa	Munich	Montreal		900
Lufthansa	Munich	Newark		900
Lufthansa	Munich	San Francisco		900
Malaysia	Kuala Lumpur	Tokyo Narita		900
Malaysia	Kuala Lumpur	London Heathrow		900
Philippine Airlines	Manila	London Heathrow		900
Philippine Airlines	Manila	New York JFK		900
Philippine Airlines	Manila	Toronto		900

Table B.4: A350 City-pairs (4/5)

Airline	Origin	Destination	Destination 2	Type
Qatar Airways	Doha	Addis Ababa		900
Qatar Airways	Doha	Cape Town		900
Qatar Airways	Doha	Johannesburg		900
Qatar Airways	Doha	Bangalore		1000
Qatar Airways	Doha	Chennai		900
Qatar Airways	Doha	Delhi		900
Qatar Airways	Doha	Hong Kong		900
Qatar Airways	Doha	Jakarta		900
Qatar Airways	Doha	Kochi		900
Qatar Airways	Doha	Kuala Lumpur		900
Qatar Airways	Doha	Seoul Incheon		900
Qatar Airways	Doha	Singapore		900
Qatar Airways	Doha	Tokyo Narita		1000
Qatar Airways	Doha	Adelaide		900
Qatar Airways	Doha	Brisbane	Auckland	1000
Qatar Airways	Doha	Melbourne		1000
Qatar Airways	Doha	Perth		1000
Qatar Airways	Doha	Sydney		1000
Qatar Airways	Doha	Amsterdam		1000
Qatar Airways	Doha	Barcelona		900
Qatar Airways	Doha	Berlin		900
Qatar Airways	Doha	Brussels		900
Qatar Airways	Doha	Copenhagen		900
Qatar Airways	Doha	Edinburgh		900
Qatar Airways	Doha	Frankfurt		900
Qatar Airways	Doha	London Heathrow		900
Qatar Airways	Doha	Madrid		900
Qatar Airways	Doha	Milan Malpensa		900
Qatar Airways	Doha	Munich		900
Qatar Airways	Doha	Oslo		900
Qatar Airways	Doha	Rome Fiumicino		900
Qatar Airways	Doha	Stockholm Arlanda		900
Qatar Airways	Doha	Zurich		900
Qatar Airways	Doha	Boston		900
Qatar Airways	Doha	Chicago O'Hare		900
Qatar Airways	Doha	Dallas Ft Worth		1000
Qatar Airways	Doha	Houston Intercontinental		1000
Qatar Airways	Doha	Los Angeles		1000
Qatar Airways	Doha	Miami		900
Qatar Airways	Doha	Montreal		900
Qatar Airways	Doha	New York JFK		1000
Qatar Airways	Doha	San Francisco		900
Qatar Airways	Doha	Washington Dulles		1000
Qatar Airways	Doha	Sao Paulo Guarulhos		1000
SAS Scandinavian Airlines	Copenhagen	Shanghai Pudong		900
SAS Scandinavian Airlines	Copenhagen	Chicago O'Hare		900
SAS Scandinavian Airlines	Copenhagen	Newark		900
SAS Scandinavian Airlines	Copenhagen	San Francisco		900
Sichuan Airlines	Chengdu	Hangzhou	Los Angeles International	900
Sichuan Airlines	Chengdu	Jinan		900
Sichuan Airlines	Chengdu	Jinan	Los Angeles International	900
Sichuan Airlines	Chengdu	Nanjing		900

Table B.5: A350 City-pairs (5/5)

Airline	Origin	Destination	Destination 2	Type
Sichuan Airlines	Chengdu	Shanghai Pudong		900
Sichuan Airlines	Chengdu	Urumqi		900
Sichuan Airlines	Chengdu	Xiamen		900
Singapore Airlines	Singapore	Johannesburg		900
Singapore Airlines	Singapore	Dhaka		900
Singapore Airlines	Singapore	Hanoi		900
Singapore Airlines	Singapore	Hong Kong		900
Singapore Airlines	Singapore	Jakarta		900
Singapore Airlines	Singapore	Kuala Lumpur		900
Singapore Airlines	Singapore	Manila		900
Singapore Airlines	Singapore	Osaka Kansai		900
Singapore Airlines	Singapore	Adelaide		900
Singapore Airlines	Singapore	Auckland		900
Singapore Airlines	Singapore	Brisbane		900
Singapore Airlines	Singapore	Christchurch		900
Singapore Airlines	Singapore	Melbourne		900
Singapore Airlines	Singapore	Sydney		900
Singapore Airlines	Singapore	Sydney	Brisbane	900
Singapore Airlines	Singapore	Amsterdam Schiphol		900
Singapore Airlines	Singapore	Copenhagen		900
Singapore Airlines	Singapore	Frankfurt		900
Singapore Airlines	Singapore	Istanbul		900
Singapore Airlines	Singapore	London Heathrow		900
Singapore Airlines	Singapore	Milan Malpensa	Barcelona	900
Singapore Airlines	Singapore	Paris Charles de Gaulle		900
Singapore Airlines	Singapore	Zurich		900
Singapore Airlines	Singapore	Los Angeles		900
Singapore Airlines	Singapore	New York JFK		900
Thai Airways	Bangkok Suvarnabhumi	Nagoya Chubu		900
Thai Airways	Bangkok Suvarnabhumi	Taipei Taoyuan		900
Thai Airways	Bangkok Suvarnabhumi	Melbourne		900
Thai Airways	Bangkok Suvarnabhumi	Brussels		900
Thai Airways	Bangkok Suvarnabhumi	Copenhagen		900
Thai Airways	Bangkok Suvarnabhumi	Frankfurt		900
Thai Airways	Bangkok Suvarnabhumi	London Heathrow		900
Turkish Airlines	Istanbul	Ankara		900
Turkish Airlines	Istanbul	Antalya		900
Turkish Airlines	Istanbul	London Heathrow		900
Virgin Atlantic	London Heathrow	Johannesburg		1000
Virgin Atlantic	London Heathrow	Lagos		1000
Virgin Atlantic	London Heathrow	Atlanta		1000
Virgin Atlantic	London Heathrow	Los Angeles International		1000
Virgin Atlantic	London Heathrow	New York JFK		1000
Virgin Atlantic	London Heathrow	San Francisco		1000
Virgin Atlantic	London Heathrow	Bridgetown		1000

C

APPENDIX C: ALTITUDE EFFECTS

This appendix contains the temperature change plots supporting the altitude analysis as discussed in section 4.2.2:

- At 13000 m altitude: fig. C.1 and fig. C.2
- At 12000 m altitude: fig. C.3 and fig. C.4
- At 11000 m altitude: fig. C.5 and fig. C.6
- At 10000 m altitude: fig. C.7 and fig. C.8
- At 9000 m altitude: fig. C.9 and fig. C.10

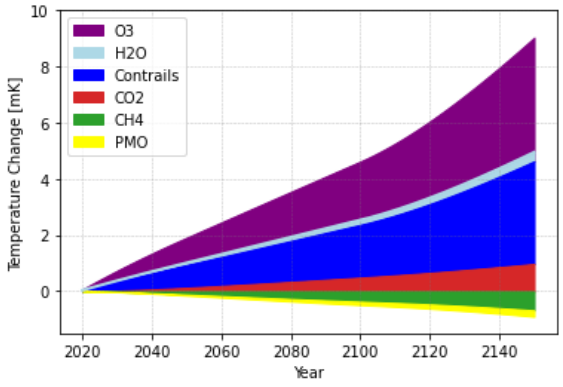

Figure C.1: A350: Temperature change at 13000 m altitude

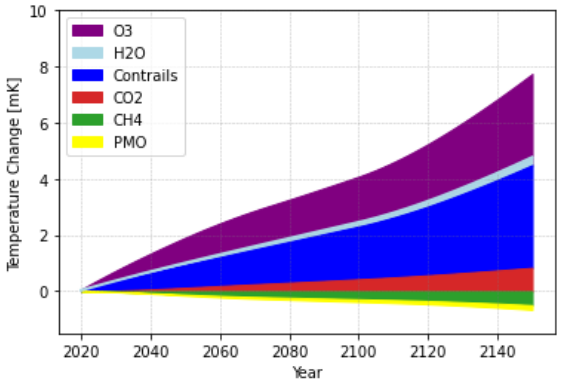

Figure C.2: Flying V: Temperature change at 13000 m altitude

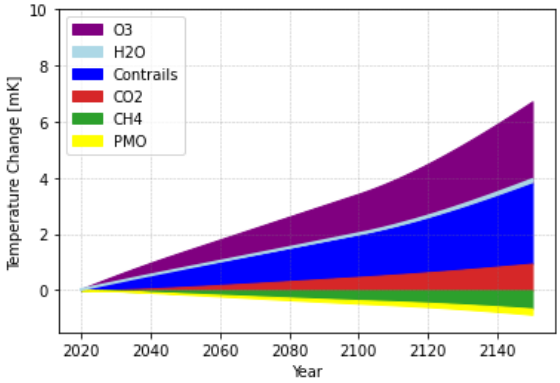

Figure C.3: A350: Temperature change at 12000 m altitude

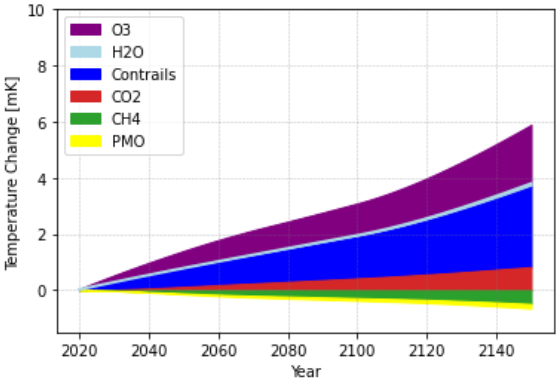

Figure C.4: Flying V: Temperature change at 12000 m altitude

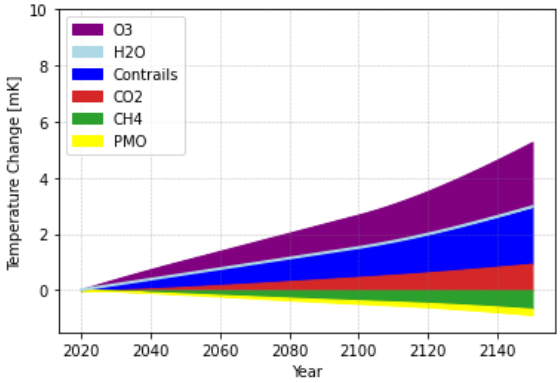

Figure C.5: A350: Temperature change at 11000 m altitude

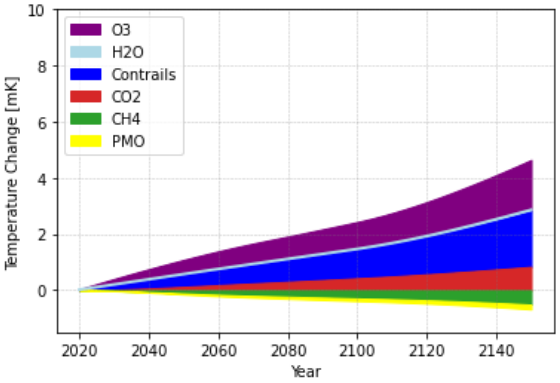

Figure C.6: Flying V: Temperature change at 11000 m altitude

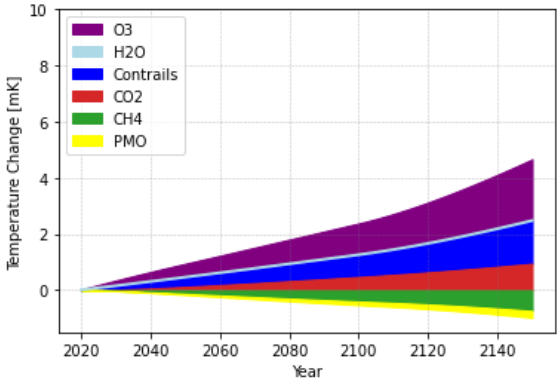

Figure C.7: A350: Temperature change at 10000 m altitude

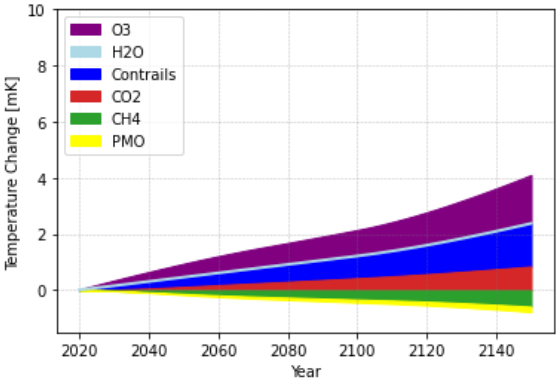

Figure C.8: Flying V: Temperature change at 10000 m altitude

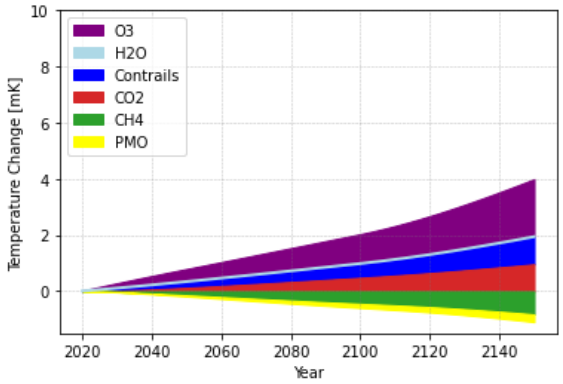

Figure C.9: A350: Temperature change at 9000 m altitude

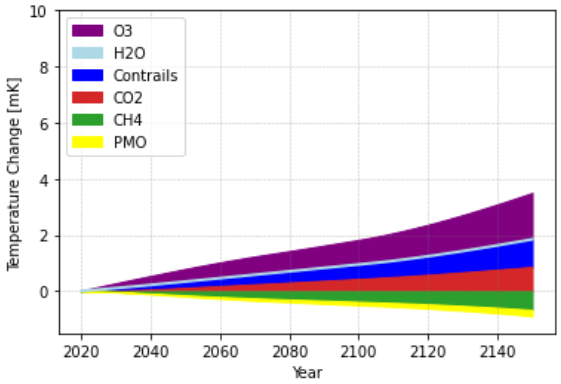

Figure C.10: Flying V: Temperature change at 9000 m altitude

D

APPENDIX D: UNCERTAINTIES

In this appendix, the histograms showing the probability densities of de individual climate agents are documented:

- CO_2 is shown in fig. D.1 and fig. D.2
- H_2O is shown in fig. D.3 and fig. D.4
- O_3 is shown in fig. D.5 and fig. D.6
- CH_4 is shown in fig. D.7 and fig. D.8
- PMO is shown in fig. D.9 and fig. D.10
- Contrails is shown in fig. D.11 and fig. D.12

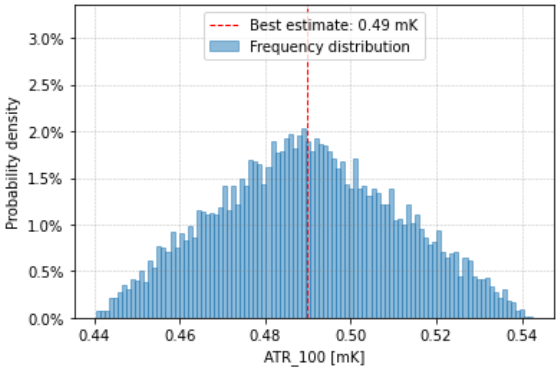

Figure D.1: Altitude effects A350-900 - CO_2

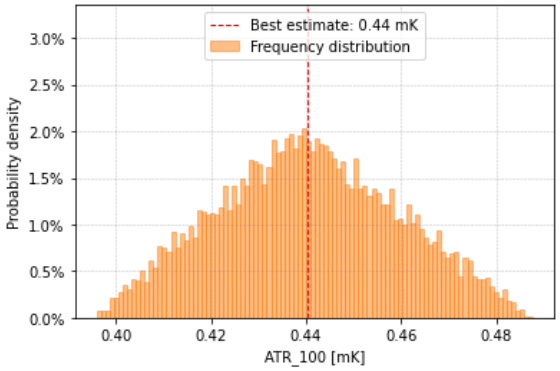

Figure D.2: Altitude effects Flying V-900 -CO_2

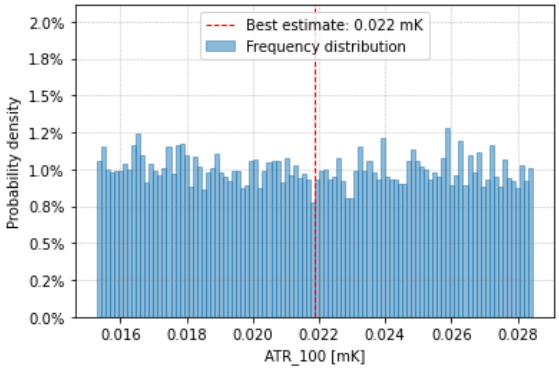

Figure D.3: Altitude effects A350-900 - H_2O

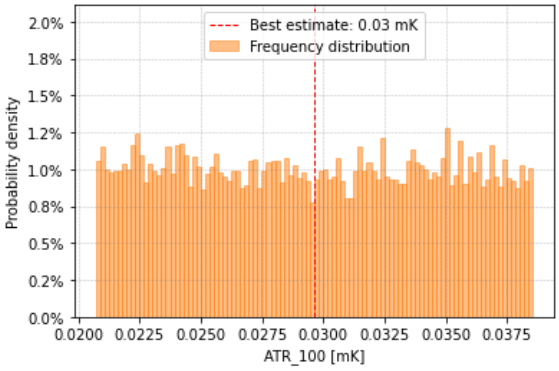

Figure D.4: Altitude effects Flying V-900 -H_2O

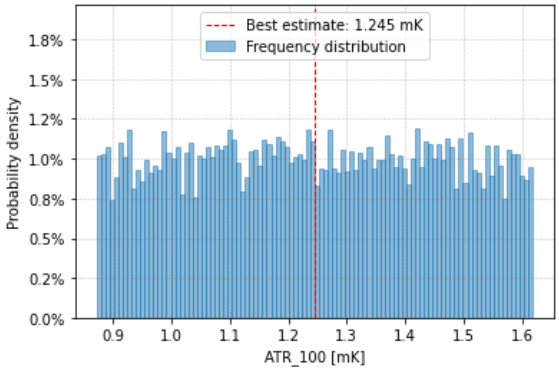

Figure D.5: Altitude effects A350-900 - O_3

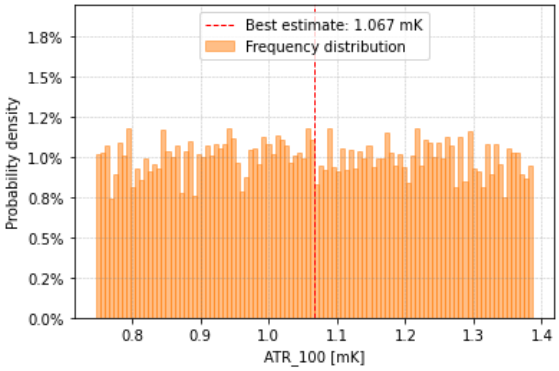

Figure D.6: Altitude effects Flying V-900 - O_3

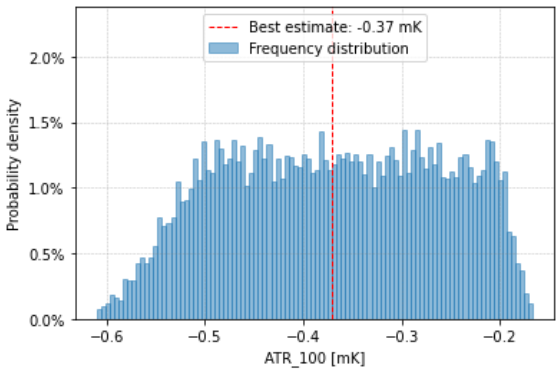

Figure D.7: Altitude effects A350-900 - CH_4

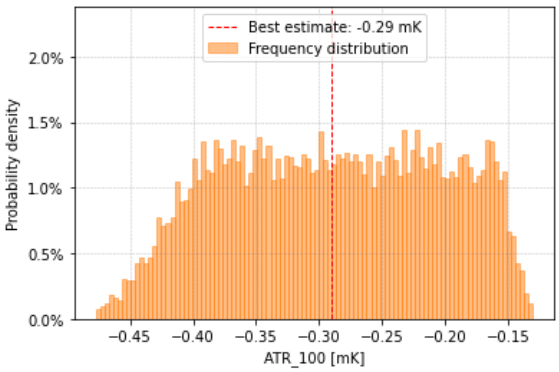

Figure D.8: Altitude effects Flying V-900 - CH_4

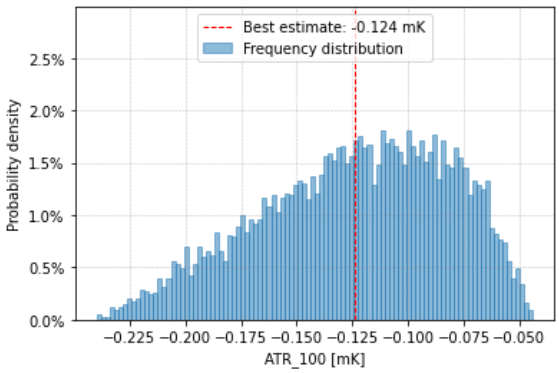

Figure D.9: Altitude effects A350-900 - PMO

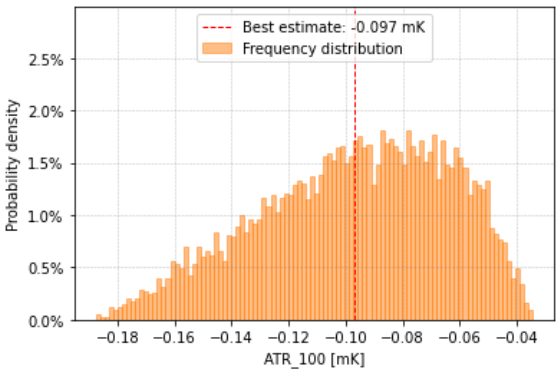

Figure D.10: Altitude effects Flying V-900 - PMO

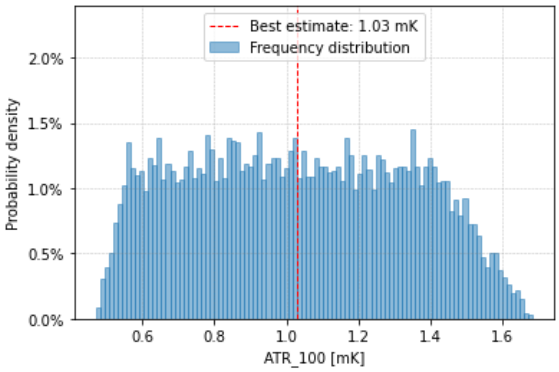

Figure D.11: Altitude effects A350-900 - Contrails

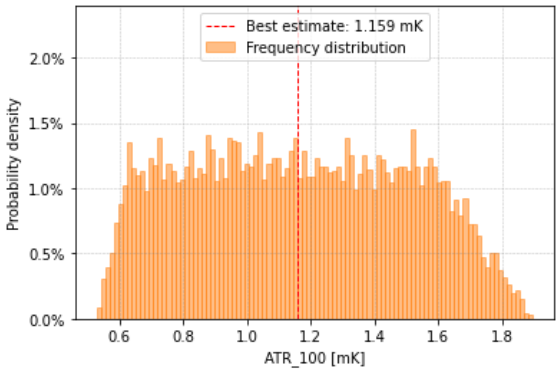

Figure D.12: Altitude effects Flying V-900 - Contrails

E

Appendix E: Verification

Figure E.1 shows the verification of the performance model with identical drag polar values as Piano-X.

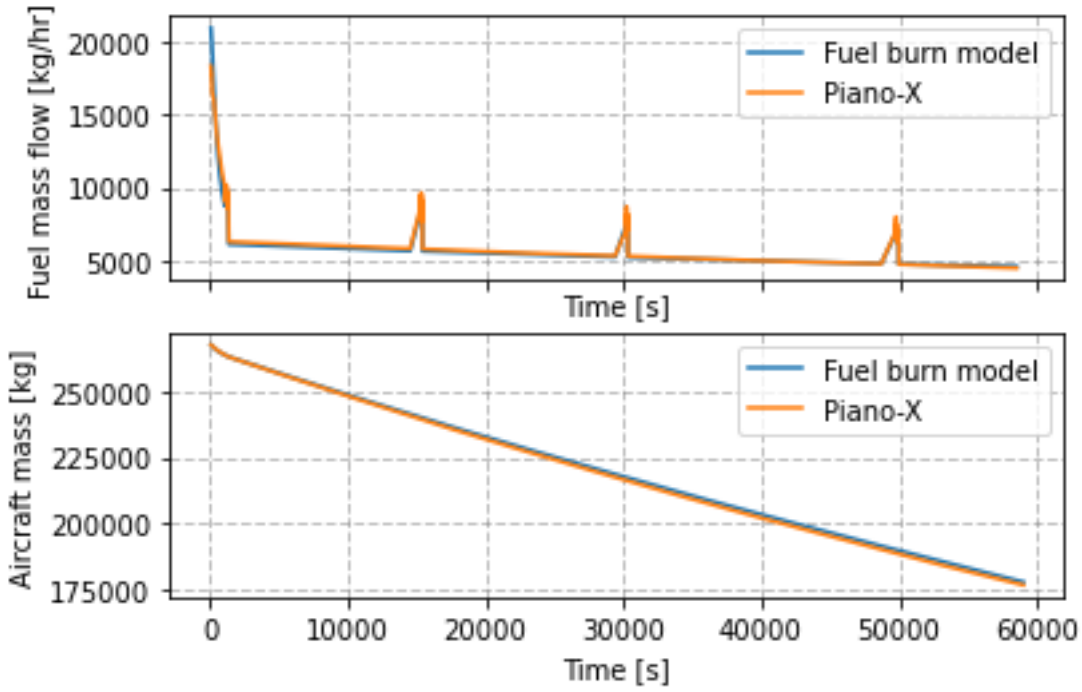

Figure E.1: Verification performance model vs. Piano-X, identical drag polar